Site-Specific Structure at Multiple Length Scales in Kagome Quantum Spin Liquid Candidates

Rebecca W. Smaha,[1,2,*] Idris Boukahil,[3,4,†] Charles J. Titus,[3,†] Jack Mingde Jiang,[1,5,†] John P. Sheckelton,[1] Wei He,[1,6] Jiajia Wen,[1] John Vinson,[7] Suyin Grass Wang,[8] Yu-Sheng Chen,[8] Simon J. Teat,[9] Thomas P. Devereaux,[1,6] C. Das Pemmaraju,[4] and Young S. Lee[1,5,‡]

[1] *Stanford Institute for Materials and Energy Sciences, SLAC National Accelerator Laboratory, Menlo Park, California 94025, USA*
[2] *Department of Chemistry, Stanford University, Stanford, California 94305, USA*
[3] *Department of Physics, Stanford University, Stanford, California 94305, USA*
[4] *Theory Institute for Materials and Energy Spectroscopies, SLAC National Accelerator Laboratory, Menlo Park, California 94025, USA*
[5] *Department of Applied Physics, Stanford University, Stanford, California 94305, USA*
[6] *Department of Materials Science and Engineering, Stanford University, Stanford, California 94305, USA*
[7] *Material Measurement Laboratory, National Institute of Standards and Technology, 100 Bureau Drive, Gaithersburg, MD 20899*
[8] *NSF's ChemMatCARS, Center for Advanced Radiation Sources, c/o Advanced Photon Source/ANL, The University of Chicago, Argonne, Illinois 60439, USA*
[9] *Advanced Light Source, Lawrence Berkeley National Laboratory, Berkeley, California 94720, USA*

(Dated: November 14, 2020)

Realizing a quantum spin liquid (QSL) ground state in a real material is a leading issue in condensed matter physics research. In this pursuit, it is crucial to fully characterize the structure and influence of defects, as these can significantly affect the fragile QSL physics. Here, we perform a variety of cutting-edge synchrotron X-ray scattering and spectroscopy techniques, and we advance new methodologies for site-specific diffraction and L-edge Zn absorption spectroscopy. The experimental results along with our first-principles calculations address outstanding questions about the local and long-range structures of the two leading kagome QSL candidates, Zn-substituted barlowite ($Cu_3Zn_xCu_{1-x}(OH)_6FBr$) and herbertsmithite ($Cu_3Zn(OH)_6Cl_2$). On all length scales probed, there is no evidence that Zn substitutes onto the kagome layers, thereby preserving the QSL physics of the kagome lattice. Our calculations show that antisite disorder is not energetically favorable and is even less favorable in Zn-barlowite compared to herbertsmithite. Site-specific X-ray diffraction measurements of Zn-barlowite reveal that Cu^{2+} and Zn^{2+} selectively occupy distinct interlayer sites, in contrast to herbertsmithite. Using the first measured Zn L-edge inelastic X-ray absorption spectra combined with calculations, we discover a systematic correlation between the loss of inversion symmetry from pseudo-octahedral (herbertsmithite) to trigonal prismatic coordination (Zn-barlowite) with the emergence of a new peak. Overall, our measurements suggest that Zn-barlowite has structural advantages over herbertsmithite that make its magnetic properties closer to an ideal QSL candidate: its kagome layers are highly resistant to nonmagnetic defects while the interlayers can accommodate a higher amount of Zn substitution.

I. INTRODUCTION

Quantum spin liquid (QSL) materials exhibit an unusual magnetic ground state that is characterized by long-range quantum entanglement of the spins without long-range magnetic order.[1] While they have been theoretically predicted for many years,[2, 3] experimental breakthroughs have only begun to occur in the past ≈15 years.[4] A promising host for a QSL ground state is the kagome lattice, which consists of corner-sharing triangles. Antiferromagnetic (AF) spins on a kagome lattice exhibit a high level of geometric magnetic frustration; for spin $S = \frac{1}{2}$ nearest-neighbor Heisenberg systems there is no magnetic order, and the ground state is believed to be a QSL.[5–12] Many of the predicted signatures of QSL physics occur at low energy scales much smaller than the magnetic exchange J.

In order to make deep contact between theory and experiment, it has become increasingly clear that a quantitative accounting of the defect structure of the materials must be made. The leading kagome QSL candidate material is the synthetic mineral herbertsmithite, $Cu_3Zn(OH)_6Cl_2$; it has a layered structure crystallizing in rhombohedral space group $R\bar{3}m$ that consists of perfect 2D kagome lattices of $S = \frac{1}{2}$ Cu^{2+} cations separated by non-magnetic Zn^{2+} and Cl^- ions.[4, 13–15] The presence and amount of magnetic "impurities" of Cu^{2+} between the kagome layers has been the subject of debate, as they obscure measurement of the fundamental physics of the QSL ground state.[16] Standard crystallographic techniques such as X-ray and neutron diffrac-

* rsmaha@stanford.edu
† These authors contributed equally to this work
‡ youngsl@stanford.edu

tion cannot accurately differentiate Cu and Zn as their scattering factors and ionic radii are nearly identical. In order to distinguish site occupancies of these two elements in herbertsmithite, Freedman *et al.* used a novel approach to X-ray anomalous diffraction, in conjunction with extended X-ray absorption fine structure (EXAFS) measurements, to show that up to 15% Cu^{2+} mixes onto the pseudo-octahedral interlayer Zn^{2+} sites despite best synthetic attempts to substitute a full equivalent of interlayer Zn, leading to a formula of approximately $Cu_3Zn_{0.85}Cu_{0.15}(OH)_6Cl_2$.[17] In addition, it should be highly unlikely for Zn^{2+} to mix onto the kagome sites as these sites are highly distorted (CuO_4Cl_2 elongated octahedra). This coordination is consistent with the Jahn-Teller activity of Cu^{2+}, but Zn^{2+} as a Jahn-Teller inactive ion should prefer a more octahedral coordination. Anomalous diffraction and EXAFS confirmed this assignment of negligible mixing.[17]

The complications with herbertsmithite have spurred research into related materials in order to develop novel QSL candidates. Another recently discovered mineral with kagome planes of Cu^{2+} is barlowite ($Cu_4(OH)_6FBr$), which crystallizes in hexagonal space group $P6_3/mmc$.[18–25] There are three main structural differences between barlowite and herbertsmithite. 1) The stacking of the kagome planes in barlowite is AA, whereas it is ABCA in herbertsmithite. 2) The interlayer metal coordination is different—barlowite's Cu^{2+}s are disordered over three symmetry-equivalent sites in distorted trigonal prismatic coordination (point group C_{2v}). This coordination is relatively rare for Cu^{2+}, although it occurs in several organometallic complexes and related minerals such as the isostructural mineral claringbullite.[26, 27] However, in herbertsmithite, both the interlayer Zn^{2+} and impurity Cu^{2+} occupy the same centered position (point group D_{3d}). 3) At low temperature, crystallographic studies show that herbertsmithite maintains its perfect kagome planes and exhibits no symmetry lowering,[4, 17] but barlowite has a clear structural phase transition at $T \approx 265$ K to orthorhombic ($Pnma$) or lowered hexagonal symmetry ($P6_3/m$), depending on the synthesis technique.[28] However, standard crystallography yields the average, long-range structure; recent non-crystallographic evidence has pointed to a possible symmetry-lowering local distortion in herbertsmithite,[29–33] although this is still under debate.

While in barlowite the Cu^{2+} cations between the kagome layers lead to long-range magnetic order, substituting Zn^{2+} into the compound produces a new QSL candidate, Zn-substituted barlowite ($Cu_3Zn_xCu_{1-x}(OH)_6FBr$). This is an intriguing material to study as first-principles calculations predict significantly fewer magnetic Cu^{2+} impurities on the interlayer site than in herbertsmithite.[34, 35] In polycrystalline samples, nearly a full equivalent of Zn can be introduced.[24, 28, 36, 37] We have recently synthesized the first single crystals of Zn-barlowite with no magnetic order with a Zn substitution level of $x \approx 0.5$, and the structure of this compound contains two distinct interlayer sites—the set of three symmetry-equivalent off-center sites observed in barlowite (point group C_{2v}) and a centered site (point group D_{3h}).[28] This motif is also observed in the rare single crystals found in our previously reported polycrystalline growths[28] but has never been observed in herbertsmithite, indicating a fundamental difference in the interlayer behavior between the two compounds. Here, we synthesize deuterated single crystals of Zn-barlowite for the first time, achieving a Zn substitution of $x = 0.52$; this will enable future neutron scattering experiments.

To obtain precise information on the presence of defects, we perform synchrotron-based spectroscopic and scattering experiments as well as first-principles simulations on Zn-barlowite and herbertsmithite. We study Zn-barlowite with two distinct levels of Zn substitution, $x \approx 0.5$ and $x = 0.95$, that both display QSL behavior in contrast to barlowite (the parent compound), which exhibits long-range magnetic order either at $T = 15$ K with orthorhombic $Pnma$ symmetry or at $T = 6$ K with hexagonal $P6_3/m$ symmetry (denoted barlowite **1** and **2**, respectively), as described in Ref [28]. The results allow us to make important claims regarding the influence of disorder on the QSL behavior. First, the evidence shows that Zn does not substitute onto the kagome sites. K-edge EXAFS data, a common element-specific technique that measures local structure, are consistent with the lack of anti-site disorder in either herbertsmithite or Zn-barlowite. Site-specific X-ray anomalous diffraction measurements, which probe the long-range crystal structure, definitively determine the Cu/Zn site occupancies of the kagome site, further supporting this conclusion. In addition, they indicate that the two distinct interlayer sites are selectively occupied by Cu or Zn even in highly Zn-substituted barlowite.

Using powerful new superconducting transition edge sensor detector technology,[38] high-resolution Cu and Zn L-edge X-ray absorption near edge spectroscopy (XANES) measurements of the barlowite family and herbertsmithite are performed, including the first reported Zn L-edge resonant inelastic X-ray scattering (RIXS) data. Comparing the experimental Zn L-edge spectra to first-principles OCEAN [39] simulations where Zn has been placed onto either the interlayer site or the kagome site indicates that Zn^{2+} does not occupy the kagome site. Instead, it occupies a centered interlayer site in both Zn-substituted barlowite and herbertsmithite. The simulated and experimental spectra reveal a clear distinction between the local symmetry of the interlayer Zn^{2+} in these two compounds; we show that trigonal prismatic and pseudo-octahedral coordination can be distinguished in Zn L-edge XANES. We find that while the local symmetry of the dilute Cu^{2+} defects are different in Zn-barlowite compared to herbertsmithite, the bulk magnetic properties remain very similar,[28] showing that the kagome QSL is robust to this aspect of the

material-specific disorder.

II. METHODS

Protonated and deuterated low-temperature orthorhombic barlowite powder (denoted **1**), low-temperature hexagonal barlowite crystals (denoted **2**), polycrystalline Zn-substituted barlowite with $x = 0.95$ (denoted $\mathbf{Zn}^{\mathrm{H}}_{0.95}$ and $\mathbf{Zn}^{\mathrm{D}}_{0.95}$), and protonated single crystalline Zn-substituted barlowite with $x = 0.56$ (denoted $\mathbf{Zn}^{\mathrm{H}}_{0.56}$) were synthesized as described previously.[24, 28] Polycrystalline and single crystalline herbertsmithite were synthesized as described previously.[4, 40]

Deuterated single crystalline Zn-substituted barlowite (denoted $\mathbf{Zn}^{\mathrm{D}}_{0.52}$) was prepared by sealing 0.213 g of CuF_2, 0.796 g of ZnF_2, and 1.641 g of LiBr in a 23 mL PTFE-lined stainless steel autoclave with 15 mL D_2O. The autoclave was heated over 3 hours to 220 °C and held for 120 hours, then cooled to 80 °C over 48 hours. It was held at 80 °C for 72 hours before being cooled to room temperature over 24 hours. The product was recovered by filtration and washed with DI H_2O, yielding Zn-barlowite crystals mixed with polycrystalline LiF, which was removed by sonication in acetone.

Powder X-ray diffraction (PXRD) data were collected on $\mathbf{Zn}^{\mathrm{D}}_{0.52}$ at beamline 11-BM at the Advanced Photon Source (APS), Argonne National Laboratory, at $T = 90$ K and $T = 295$ K using an energy of 30 keV. Crystalline samples were crushed into a powder and measured in Kapton capillaries. Rietveld refinements were performed using GSAS-II.[41] Atomic coordinates and isotropic atomic displacement parameters were refined for each atom; site occupancy was also refined for the interlayer site when appropriate. Deuterium was excluded.

Single crystal x-ray diffraction (SCXRD) data sets were collected at $T = 100$ K at NSF's ChemMatCARS beamline 15-ID at the APS using a Bruker APEX II detector and at beamline 12.2.1 at the Advanced Light Source (ALS), Lawrence Berkeley National Laboratory, using a Bruker D85 diffractometer equipped with a Bruker PHOTON II detector. For structure determination, data sets were collected at 30 keV for protonated $\mathbf{Zn}^{\mathrm{H}}_{0.56}$ (APS) and 17 keV for deuterated $\mathbf{Zn}^{\mathrm{D}}_{0.52}$ and $\mathbf{Zn}^{\mathrm{D}}_{0.95}$ (ALS). The data were integrated and corrected for Lorentz and polarization effects using SAINT and corrected for absorption effects using SADABS.[42] The structures were solved using intrinsic phasing in APEX3 and refined using the SHELXTL and OLEX2 software.[43, 44] Hydrogen atoms were inserted at positions of electron density near the oxygen atom and were refined with a fixed bond length and an isotropic thermal parameter 1.5 times that of the attached oxygen atom. Thermal parameters for all other atoms were refined anisotropically. Further crystallographic information can be found in Ref. [28].

For the anomalous diffraction measurements, fluorescence X-ray absorption spectra (XAS) were collected for each sample near the Cu and Zn K-edges to determine the absorption edge energies. Additional SCXRD data sets were collected on and around the Cu and Zn K-edges (see Table S9). Quantification of the anomalous scattering factors was done using modified software from Ref. [17]. The software was updated to support additional symmetry operations as well as fractionally occupied sites, which are both present in our samples. Using the crystal structure solved at high energy, the software refined the wavelength dependent terms of the atomic scattering factor, f' and f'', by minimizing $wR_2(F^2)$ against the SCXRD data at each X-ray energy. The software was modified to allow for simultaneous refinement of three atomic sites. In total, seven parameters were refined: an overall structure factor and f' and f'' for each site (kagome, centered interlayer, and off-center interlayer). The refined values are compared against the calculated values of f' to quantify the degree of Zn-Cu mixing at each site. The calculated values, f'_c, are obtained from tabulated data[45] of anomalous scattering factors calculated by Cromer and Liberman's method.[46] The relative occupation of species α at site i, p_i^α, is calculated assuming the measured f'_i is from a linear combination of f'_c of atoms present on that site. For example, to determine Zn occupation on the kagome site, we solve for $p^{Zn}_{kagome} f'^{Zn}_c + (1 - p^{Zn}_{kagome}) f'^{Cu}_c = f'_{kagome}$.

EXAFS measurements were performed in transmission and fluorescence yield mode at beamline 7-3 at the Stanford Synchrotron Radiation Lightsource (SSRL), SLAC National Accelerator Laboratory. The X-ray beam was monochromatized by a Si(220) double crystal monochromator at $\phi = 0$ orientation and detuned by 50% to reject harmonics. The beam size was chopped to 1 mm (v) by 10 mm (h) before the sample. Samples were ground to a powder, diluted in BN, and packed into sample holders, which were kept at $T = 10$ K during the measurements. Incident and transmitted flux were measured via ionization chambers, and the beam energy was calibrated using the transmission of a Cu or Zn foil downstream from the sample. Fluorescence was detected at 90° using a PIPS detector with a $Z - 1$ filter (Ni for Cu measurements and Cu for Zn measurements) and Soller slits in order to reduce background fluorescence. The Athena EXAFS package[47] was used to align and calibrate data and fit a spline to the background. Cu measurements were aligned to the first inflection point of the Cu foil, which was assumed to be at 8979 eV. Zn measurements were aligned to the first inflection point of Zn foil, assumed to be at 9659 eV. The Artemis package[47] was used to fit data using paths calculated by FEFF6.[48] Fluorescence yield spectra were used for all samples except for the Cu EXAFS of polycrystalline samples (barlowite **1** and $\mathbf{Zn}^{\mathrm{D}}_{0.95}$), which used transmission data.

High resolution Cu and Zn L_3-edge XANES measurements were carried out at room temperature at SSRL beamline 10-1. Samples were pelletized with BN or KBr and then attached to an aluminum sample holder using carbon tape. Measurements were carried out under high

vacuum conditions of $\approx 2.7 \times 10^{-6}$ Pa ($\approx 2 \times 10^{-8}$ Torr) with a ring current of 500 mA. The synchrotron radiation was monochromatized using the beamline's 1000 line/mm monochromator with entrance and exit slits of 27 μm. A transition edge sensor (TES) spectrometer[38] was used to collect resonant inelastic X-ray scattering (RIXS) planes with a resolution of 2 eV. The energy measured by the TES was calibrated by periodically measuring a reference sample of graphite, BN, Fe_2O_3, NiO, CuO, and ZnO, which provide a stable set of emission lines. From the RIXS planes we extracted the L-α and L-β lines, leading to separate L_2 and L_3 edge partial-fluorescence-yield XAS.

Theoretical simulations on the Cu and Zn L-edges were performed on barlowite (the high-temperature hexagonal structure in space group $P6_3/mmc$), idealized $\mathbf{Zn}_{0.95}$ ($ZnCu_3(OH)_6FBr$), and idealized herbertsmithite ($ZnCu_3(OH)_6Cl_2$) using the crystallographically-determined structures[17, 24, 28] as a starting point. To simplify the calculations for $\mathbf{Zn}_{0.95}$ and herbertsmithite, full occupancy of Zn^{2+} on the respective centered interlayer site of each compound and full occupancy of Cu^{2+} on the kagome sites were used. For barlowite, a single off-center (C_{2v}) configuration was chosen for the interlayer Cu^{2+} cation, ignoring the site occupancy disorder. Upon structural relaxation, the interlayer Cu^{2+} kept its off-center position. Models using Zn substituted on a kagome site (stoichiometrically equivalent to the interlayer Zn models) were constructed such that there is one Zn^{2+} per kagome layer. Structural relaxations were performed using density functional theory (DFT) with projector-augmented wave pseudopotentials as implemented in the Vienna *ab initio* simulation package (VASP) code.[49–52] The PBEsol functional [53] was employed with an on-site Coulomb repulsion U set to 5 eV to account for electronic correlations in Mott-Hubbard systems. All degrees of freedom were allowed to relax until the change in energy per ion was less than 1×10^{-5} eV using a $4 \times 4 \times 4$ Γ-centered k-point sampling mesh and a plane wave cut-off energy of 520 eV.

The OCEAN package,[39, 54] which solves the Bethe-Salpeter equation (BSE) for core-level excitations, was employed to calculate the Cu and Zn L-edge spectra. The BSE is solved in conjunction with the ground state electronic structure obtained using the local density approximation (LDA) in the plane wave basis DFT code Quantum Espresso.[55] These calculations used norm conserving pseudopotentials treating O:$2s, 2p$, F:$2s, 2p$, Cl:$3s, 3p$, Cu:[Ar]$4s^1 3d^{10}$, Zn:[Ar]$4s, 3d$, and Br:$4s, 4p$ states in the valence with a plane wave cutoff of 100 Ry. Optimized geometries obtained using the VASP code as described above were used in these simulations. Convergence was achieved with a $6 \times 6 \times 6$ k-point sampling mesh for the final state wavefunctions and a $2 \times 2 \times 2$ grid for the screened core-hole interaction. The theoretical spectra were energy aligned to the first peak in the corresponding experimental spectrum.

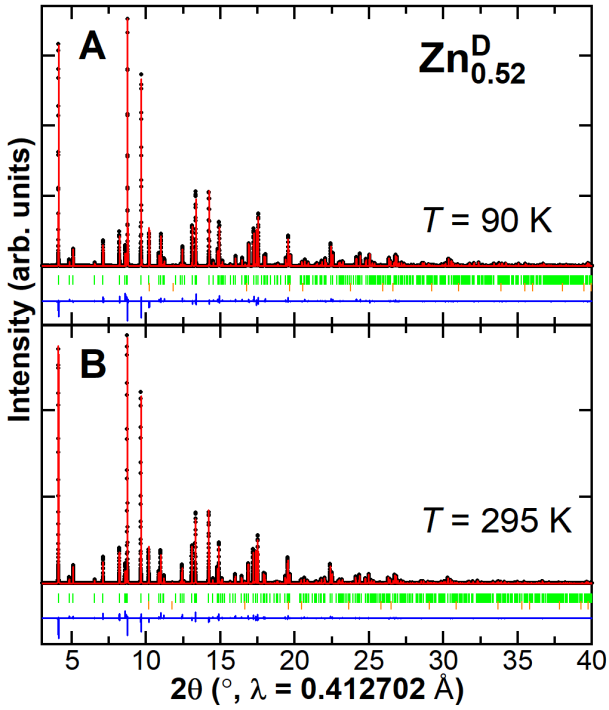

FIG. 1. Rietveld refinements of synchrotron PXRD data of deuterated $\mathbf{Zn}^{\mathrm{D}}_{0.52}$ at A) $T = 90$ K and B) 295 K (bottom) in space group $P6_3/mmc$. Observed (black), calculated (red), and difference (blue) plots are shown, and Bragg reflections are indicated by green tick marks. The Bragg reflections of a LiF impurity phase are marked with orange tick marks.

III. RESULTS

A. Synthesis and Crystal Structure

In this work, we report the first synthesis of deuterated single crystals of Zn-substituted barlowite, achieving a Zn substitution of $x = 0.52$ ($Cu_{3.48}Zn_{0.52}(OD)_6FBr$) as measured by inductively coupled plasma atomic emission spectroscopy (ICP-AES); the availability of these crystals will enable future neutron scattering experiments of the ground state physics of this compound. This sample is denoted $\mathbf{Zn}^{\mathrm{D}}_{0.52}$, where the superscript indicates if it is protonated or deuterated and the subscript indicates the level of Zn substitution. Rietveld refinements of synchrotron powder X-ray diffraction (PXRD) data of $\mathbf{Zn}^{\mathrm{D}}_{0.52}$ collected at $T = 90$ and 295 K are shown in Figure 1, and synchrotron single crystal x-ray diffraction (SCXRD) was performed at $T = 100$ K. Crystallographic data from these measurements are tabulated in Tables S1–S6 in the Supplemental Material.[56] The average formula from all diffraction measurements is $Cu_{3.54}Zn_{0.46}(OH)_6FBr$, consistent with the ICP-AES results.

We also investigate samples reported previously: two compositions of Zn-substituted barlowite with different levels of Zn substitution synthesized via distinct chemi-

cal reactions.[24, 28] Protonated single crystals analogous to the deuterated crystals reported here achieved a maximum Zn substitution of $x = 0.56$. This yielded the formula $Cu_{3.44}Zn_{0.56}(OH)_6FBr$ (denoted $\mathbf{Zn}^{H}_{0.56}$); detailed crystallographic studies are reported in Ref. [28]. Polycrystalline samples with $x = 0.95$ are denoted $\mathbf{Zn}_{0.95}$; this is comparable to—but higher than—the level of substitution achieved in herbertsmithite.[17] Its structure was determined by synchrotron PXRD and neutron powder diffraction (NPD).[28] A crystal, one of fewer than 15 found in the synthesis of nearly 20 g of the polycrystalline sample, was measured via synchrotron SCXRD in Ref. [28]; this is the $\mathbf{Zn}^{D}_{0.95}$ sample upon which X-ray anomalous diffraction measurements are performed here, as described in Section III C. It has non-negligible electron density on the triplicated off-center (C_{2v}) interlayer sites—approximately 5% on each, for a total of 15%—leading to an empirical formula (assuming Cu on the kagome and off-center interlayer sites and Zn on the centered interlayer site) of $Cu_{3.15}Zn_{0.85}(OD)_6FBr$. This is slightly different from the bulk formula determined by ICP-AES of $Cu_{3.05}Zn_{0.95}(OD)_6FBr$.[28] Both facts suggest that this crystal may not be representative of the bulk. However, it is valuable to test whether the structural trends observed in the samples with $x \approx 0.5$ are robust to higher Zn substitution values, and it allows a structural comparison with herbertsmithite, which has approximately the same amount of Zn substitution.

Both the $x = 0.95$ and $x \approx 0.5$ compositions of Zn-barlowite crystallize in space group $P6_3/mmc$ (No. 194) down to the lowest measured temperatures; this lack of symmetry lowering implies that their kagome lattices remain perfect and undistorted. SCXRD refinements (from this work for $\mathbf{Zn}^{D}_{0.52}$ and Ref. [28] for $\mathbf{Zn}^{H}_{0.56}$ and $\mathbf{Zn}_{0.95}$) indicate that both have two distinct sites for the interlayer metal ions (see Figure 4), but the similarity of the X-ray scattering factors of Cu and Zn makes it impossible to distinguish these elements accurately. Jahn-Teller theory provides a reasonable guess that Cu^{2+} should occupy the kagome site (which has heavily elongated CuO_4Br_2 octahedra) and the set of three off-center, distorted trigonal prismatic (C_{2v}) interlayer sites observed in all-Cu barlowite.[26] The coordination of each off-center interlayer site consists of four short and two long M–O bonds (≈2.0 and 2.4 Å, respectively). In contrast, the Jahn-Teller inactivity of Zn^{2+} should predispose it to occupy the centered interlayer site in D_{3h} point group symmetry, which has 6 equivalent M–O bond lengths (≈2.1 Å).

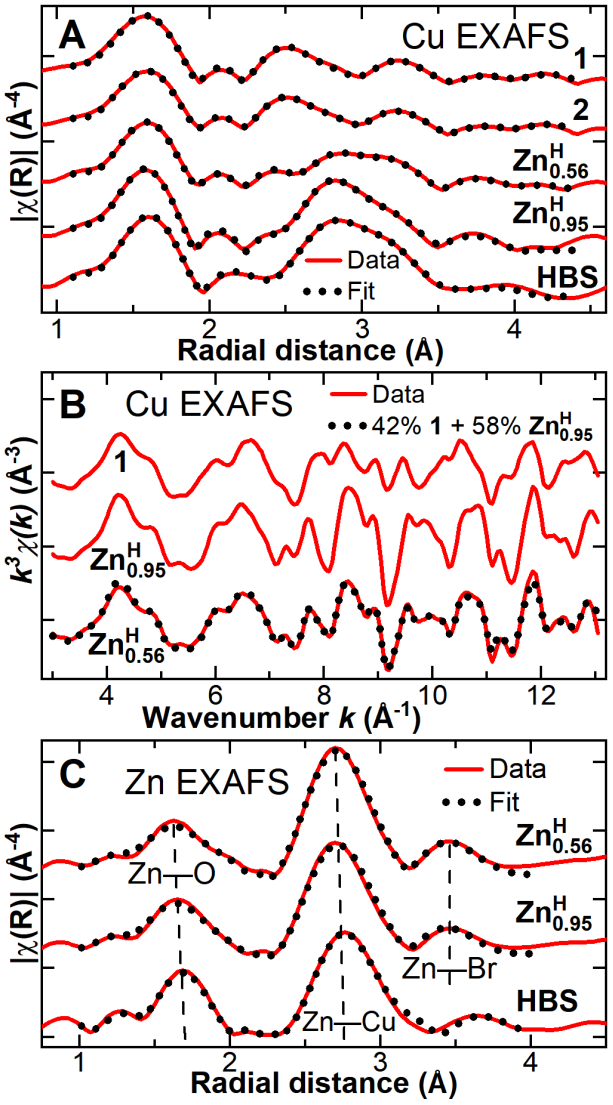

FIG. 2. A) Real-space Cu K-edge EXAFS data and fits of barlowite **1**, barlowite **2**, $\mathbf{Zn}^{H}_{0.56}$, $\mathbf{Zn}^{H}_{0.95}$, and herbertsmithite (HBS) showing the magnitude of the Fourier-transformed EXAFS ($\chi(R)$) measured at $T = 10$ K. B) Linear component fit of normalized $\mathbf{Zn}^{H}_{0.56}$ Cu EXAFS data of barlowite **1** and $\mathbf{Zn}^{H}_{0.95}$. C) Real-space Zn K-edge EXAFS data and fits to $\mathbf{Zn}^{H}_{0.56}$, $\mathbf{Zn}^{H}_{0.95}$, and herbertsmithite (HBS) measured at $T = 10$ K. The three paths for Zn-substituted barlowite are shown as dashed lines. Vertical offsets have been applied to separate the spectra.

B. EXAFS Measurements

Extended X-ray absorption fine structure (EXAFS) measurements at the Cu and Zn K-edges provide element-specific insight into the local geometry, in contrast to crystallography which gives a global picture of long-range crystalline order. Crystallographic data from Ref. [28] were used to generate the base paths and coordination numbers for the EXAFS fits. It was assumed that the kagome sites are fully occupied by Cu and that in Zn-substituted barlowite the off-center interlayer site is occupied by Cu while the centered interlayer site is occupied by Zn; further experimental validation of these assumptions will be discussed in Section III C. Fit details are discussed at greater length in the Supplemental Material and shown in Tables S7–S8. The real parts of $\chi(R)$ are shown in Figure S1.

Cu EXAFS data and fits for barlowite **1** and **2**, Zn-

barlowite $\mathbf{Zn}^{\mathrm{H}}_{0.56}$ and $\mathbf{Zn}^{\mathrm{H}}_{0.95}$, and herbertsmithite are shown in Figure 2A. Our EXAFS models reproduce the data well, capturing all significant features and confirming that the local structure is consistent with the crystallographic data. However, in contrast to the crystallography that reveals different symmetries for **1** and **2** at low temperatures (orthorhombic *Pnma* and hexagonal $P6_3/m$, respectively), their EXAFS spectra are identical, suggesting that the global symmetry differences of the long-range structures between these samples are not tied to changes in the local environment of the Cu. The differences between the $\mathbf{Zn}^{\mathrm{H}}_{0.95}$ and herbertsmithite spectra around ≈2.25 Å are due to the different bond length of Cu–Br compared to Cu–Cl. In Figure 2B, a linear component analysis of normalized Cu EXAFS data for $\mathbf{Zn}^{\mathrm{H}}_{0.56}$ is shown, confirming $\mathbf{Zn}^{\mathrm{H}}_{0.56}$ as a midpoint between barlowite **1** and $\mathbf{Zn}^{\mathrm{H}}_{0.95}$. The $\mathbf{Zn}^{\mathrm{H}}_{0.56}$ data are fit well by the expected blend of barlowite **1** and $\mathbf{Zn}^{\mathrm{H}}_{0.95}$, which indicates 42% Cu on the interlayer, consistent with the stoichiometry found via ICP-AES and the relative occupancies of the two types of interlayer sites observed crystallographically.

Figure 2C shows fits to Zn K-edge EXAFS data for $\mathbf{Zn}^{\mathrm{H}}_{0.56}$, $\mathbf{Zn}^{\mathrm{H}}_{0.95}$, and herbertsmithite; they are consistent with locating all Zn on the interlayer. Both Zn-substituted barlowite samples can be fit well with the Zn–O, Zn–Cu, and Zn–Br bond lengths expected for interlayer Zn^{2+}. Were Zn^{2+} to occupy the kagome site, the paths should differ primarily via the inclusion of a 3.3 Å Zn–Cu bond; attempting this does not improve the fit of either $\mathbf{Zn}^{\mathrm{H}}_{0.56}$ or $\mathbf{Zn}^{\mathrm{H}}_{0.95}$, and when the occupancy of this site is allowed to freely refine, it is indistinguishable from zero. In addition, our herbertsmithite Zn K-edge data are in broad agreement with a previous report, which concluded that no statistically significant amount of Zn^{2+} occupies the kagome layer.[17] The spectra of $\mathbf{Zn}^{\mathrm{H}}_{0.56}$ and $\mathbf{Zn}^{\mathrm{H}}_{0.95}$ are nearly identical, indicating that Zn^{2+} occupies the same site in both compositions.

While EXAFS paints a consistent picture of the local environment in barlowite and herbertsmithite, this approach has inherent limitations. Although EXAFS is an element-specific technique, it is not site-specific, requiring a model which averages over all sites. Within this framework, it is easy to conclude that the Zn spectra can be fit well by a model that only includes an interlayer site, but difficult to conclusively determine that Zn^{2+} is not present on the kagome site with some small occupancy, as this signal would represent a small average contribution to the EXAFS spectrum. Furthermore, the crystalline nature of these samples results in a large number of single-scattering paths—so many that it was not possible to include them all in a model and still respect the degree-of-freedom constraint imposed by the measured k-range.[57] This statistical constraint prevents the application of even more complex models. Thus, although we have demonstrated that the EXAFS of Zn-barlowite is consistent with no occupation of the kagome site by Zn^{2+} and improved upon the measurements of herbertsmithite originally performed by Ref. [17], an element-specific technique is not sufficient. Resolving conclusively which crystallographic sites within Zn-substituted barlowite are occupied by Cu^{2+} and Zn^{2+} requires a technique that is both element-specific *and* site-specific, as discussed below.

C. X-Ray Anomalous Diffraction

We performed multi-wavelength X-ray anomalous diffraction measurements to provide both element specificity and site specificity to characterize the Cu/Zn populations on kagome and interlayer sites. Similar measurements were previously employed to successfully distinguish Cu/Zn occupancy in herbertsmithite.[17] For compounds containing elements of similar Z, their atomic form factors can be indistinguishable, and therefore any site mixing between such elements cannot be effectively resolved with conventional crystallography. However, anomalous dispersion factors f' and f'' for each atomic species vary sensitively near absorption edges with changing incident X-ray energy. Combined with crystallography, one can determine the structure and elemental populations at specific crystallographic sites.

We have significantly broadened the analysis capabilities of software previously developed specifically for herbertsmithite,[17] which supported a subset of the possible symmetry operations and allowed the co-refinement of only two crystallographic sites. While the measurements require a synchrotron to tune the incident radiation and may be time consuming, anomalous diffraction is a powerful technique with potential for broad applications, particularly for distinguishing site mixing associated with doping/substitution that is commonly found in solid state compounds and condensed matter systems.

Synchrotron SCXRD data sets were collected on protonated $\mathbf{Zn}^{\mathrm{H}}_{0.56}$ and deuterated $\mathbf{Zn}^{\mathrm{D}}_{0.52}$ and $\mathbf{Zn}^{\mathrm{D}}_{0.95}$ at $T = 100$ K with energies selected around the absorption K-edges of Cu and Zn and at high energy far from these absorption edges (tabulated in Table S9). We refined f' and f'' for each site that may contain Cu or Zn (kagome, centered interlayer, and off-center interlayer) against crystal structures collected at high energy, as shown in Figure 3. For all three samples, f' shows no appreciable decline at the Zn edge for the kagome site, nor at the Cu edge for the centered interlayer site within experimental uncertainty. This demonstrates that there is no measurable Zn^{2+} mixing on the kagome site nor Cu^{2+} mixing on the centered interlayer (D_{3h}) site, consistent with Jahn-Teller theory.

The centered interlayer site is occupied by Zn in all samples. In $\mathbf{Zn}^{\mathrm{H}}_{0.56}$ and $\mathbf{Zn}^{\mathrm{D}}_{0.52}$ (Figure 3A and B), the slight dips of f' at the Zn edge for the off-center interlayer sites (in distorted trigonal prismatic coordination) puts the upper bound of Zn occupancy at ≈8% and ≈7%, respectively. In the single crystal found in the deuterated $\mathbf{Zn}^{\mathrm{D}}_{0.95}$ sample, the small atomic occupancy on each of the

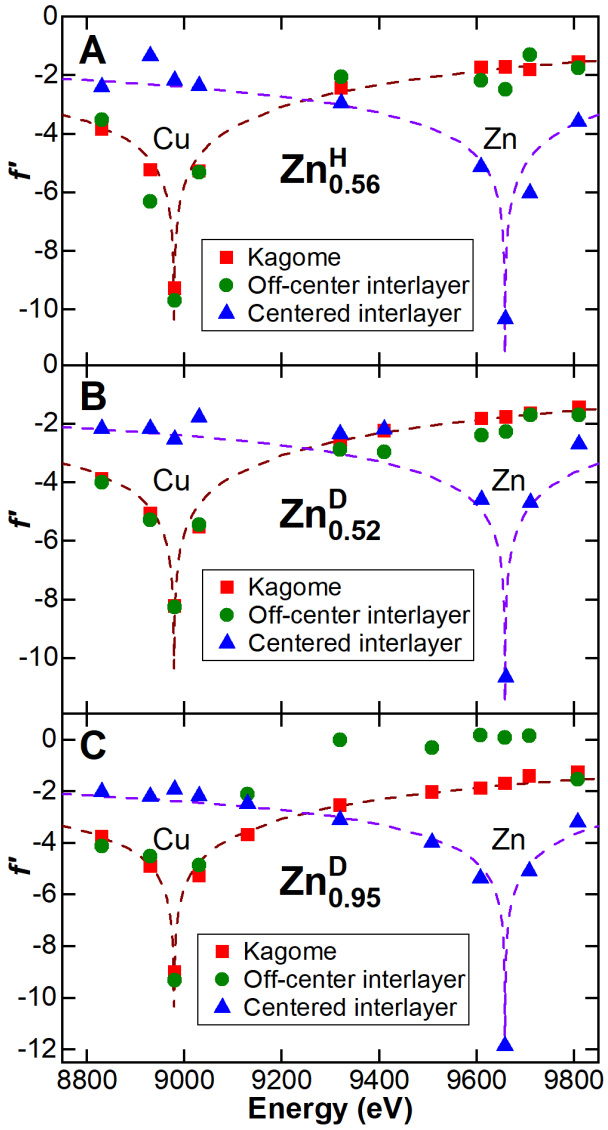

FIG. 3. Anomalous dispersion factor f' as a function of incident energy for the kagome, off-center interlayer (C_{2v}), and centered interlayer (D_{3h}) sites in A) protonated $\mathbf{Zn}^{\mathrm{H}}_{0.56}$, B) deuterated $\mathbf{Zn}^{\mathrm{D}}_{0.52}$, and C) deuterated $\mathbf{Zn}^{\mathrm{D}}_{0.95}$. The theoretical values for Cu and Zn are shown as maroon and purple dashed lines, respectively.

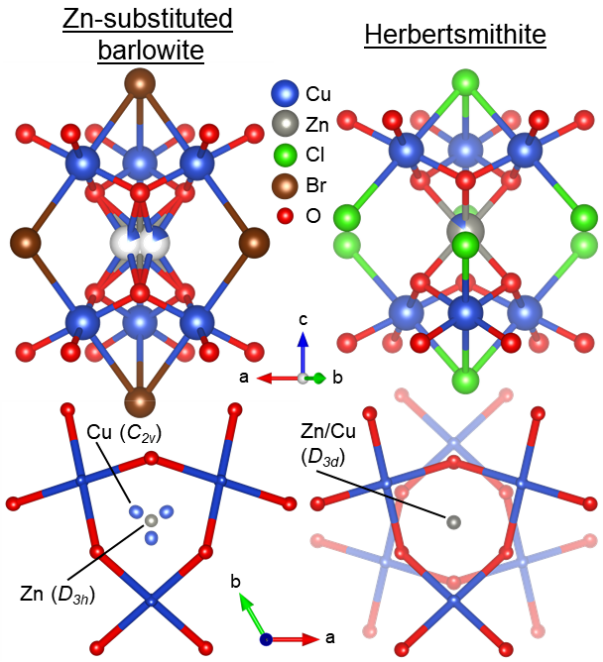

FIG. 4. Schematic comparing the structures and interlayer coordination of Zn-substituted barlowite (left) and herbertsmithite (right), visualized in VESTA.[58] Top: side-on views showing the kagome Cu^{2+}s' elongated CuO_4Br_2 or CuO_4Cl_2 octahedra and the interlayer sites. F and H (or D) atoms are not shown. Bottom: views of the interlayer metal coordination down the c-axis. The atoms are displayed as thermal ellipsoids at 90% probability. F, Br, Cl, and H (or D) atoms are not shown. We display the SCXRD structure of $\mathbf{Zn}^{\mathrm{D}}_{0.52}$ reported in this work and the herbertsmithite structure reported by Ref. [17].

three off-center interlayer sites (approximately 5%[28]) contributes to large errors in f' away from elemental edges, as shown in Figure 3C. The lack of any noticeable dip in f' on the Zn edge for the off-center interlayer sites indicates negligible presence of Zn on these sites for all three samples.

Prior Rietveld co-refinements of NPD and synchrotron PXRD data of $\mathbf{Zn}^{\mathrm{D}}_{0.95}$ produce good fits using the site assignments of Zn and Cu extracted from these anomalous diffraction results.[28] Although ICP-AES indicates that there should be approximately 5% interlayer Cu in $\mathbf{Zn}^{\mathrm{D}}_{0.95}$, it will be disordered over the three symmetry-equivalent off-center interlayer sites, leading to a mere ≈1.5% site occupancy on each site—this is nearing the detection limit of the powder diffraction data. Thus, we used a Rietveld co-refinement model of $\mathbf{Zn}^{\mathrm{D}}_{0.95}$ containing only a centered interlayer site fully occupied with Zn. The Rietveld refinements of PXRD data of protonated $\mathbf{Zn}^{\mathrm{H}}_{0.56}$ (in Ref. [28]) and deuterated $\mathbf{Zn}^{\mathrm{D}}_{0.52}$ (in Section III A) also utilize the model extracted from these anomalous diffraction results, in which the kagome site and off-center interlayer sites are fully occupied by Cu^{2+} and the centered interlayer site is fully occupied by Zn^{2+}. Cu/Zn mixing is not included in the model, consistent with the low degree of likelihood that any site is simultaneously occupied by both Cu^{2+} and Zn^{2+}, as indicated in Figure 3.

The clear existence of two types of interlayer sites in all Zn-substituted barlowite samples, and the selective occupation (consistent with Jahn-Teller predictions) of the centered and off-center sites by Zn^{2+} and Cu^{2+}, respectively, invite comparison with herbertsmithite. Since SCXRD was able to detect the presence of the off-center interlayer sites at ≈5% site occupancy in the single crystal found in the bulk $\mathbf{Zn}^{\mathrm{D}}_{0.95}$ sample, it should be able to detect similarly occupied sites in herbertsmithite. How-

ever, in herbertsmithite, only one interlayer site has been observed in all crystallographic studies (including synchrotron SCXRD, synchrotron PXRD, and NPD), and this site is occupied by a mixture of approximately 85% Zn^{2+} and 15% Cu^{2+}.[4, 17, 40, 59, 60] Figure 4 depicts the different interlayer coordination environments of Zn-barlowite and herbertsmithite in two views: side-on (in the *ac* plane) and top-down (in the *ab* plane). To further understand the nature of the differences in local coordination on the interlayer site(s) between Zn-substituted barlowite and herbertsmithite, we turned to theoretical simulations of the electronic structure.

D. Simulated and Experimental XANES Measurements

Spectra based on idealized versions of the experimental crystal structures of room-temperature ($P6_3/mmc$) barlowite, $\mathbf{Zn}_{0.95}$, and herbertsmithite (as described in Section II) were calculated using the OCEAN package and are shown in Figures 5 and 6 for the Cu and Zn L-edges, respectively, where they are referred to as the "interlayer Zn" model. To experimentally verify the simulations, we measured room temperature high-resolution X-ray absorption near edge spectra (XANES) at the Cu and Zn L-edges, which probe element-specific symmetry and electronic structure. The Cu and Zn L-edge spectra both unambiguously determine a 2+ valency, as expected. The simulations and experimental Cu L-edge spectra for barlowite, $\mathbf{Zn}^{\mathrm{H}}_{0.95}$, and herbertsmithite, in Figure 5, are in good agreement for all samples. The experimental Cu L-edge spectrum of $\mathbf{Zn}^{\mathrm{H}}_{0.56}$ is shown in Figure S2A.

We present here the first Zn L-edge absorption data collected with a transition edge sensor (TES) detector; it collects resonant inelastic X-ray scattering (RIXS) planes, allowing for the L_3-edge and L_2-edge spectra to be easily separated and measured with extremely low noise. To the extent of our knowledge, this is also the first published Zn L-edge RIXS data. Without the high energy resolution afforded by the TES, residual fluctuations from the Cu edge would overwhelm the Zn signal, making it essential for these samples in particular (as illustrated in Figure S3). The measured Zn L-edge RIXS plane of $\mathbf{Zn}^{\mathrm{H}}_{0.95}$ is depicted in Figure 6A, showing the Cu fluorescent tail and elastic scattering. An example of the two Zn L-edge components (derived from the RIXS plane) and their sum, which is what lower-resolution detectors measure, is plotted in Figure 6B for $\mathbf{Zn}^{\mathrm{H}}_{0.95}$. The analogous separated spectra for $\mathbf{Zn}^{\mathrm{H}}_{0.56}$ and herbertsmithite are plotted in Figure S2B and C. The calculated partial density of states (DOS) of idealized barlowite (room temperature), $\mathbf{Zn}_{0.95}$, and herbertsmithite, shown in Figures S4–S5, are consistent with previous results and similar across these three compounds.[20, 61–63]

The L-edge XAS of Zn^{2+} is inherently more sensitive to local structure than Cu^{2+}. In Cu^{2+}, the absorption spectrum is dominated by strong white-line transitions

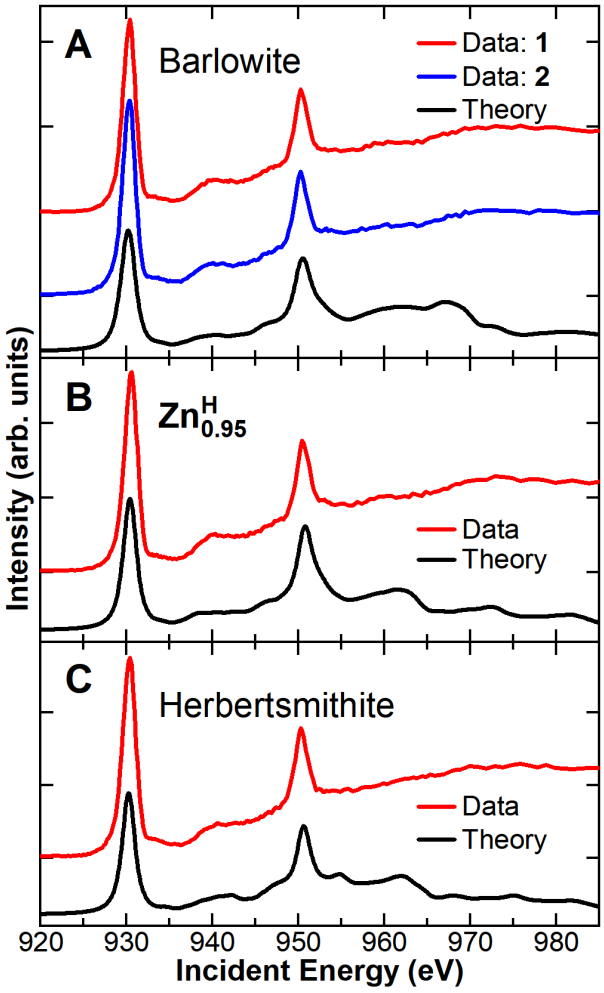

FIG. 5. Comparison of room temperature experimental Cu L-edge XANES spectra with simulations for A) barlowite **1** and **2**, B) $\mathbf{Zn}^{\mathrm{H}}_{0.95}$, and C) herbertsmithite. Vertical offsets have been applied to separate the spectra. To match the experimental spectra, the calculated spectra were broadened with a 0.6 eV Gaussian and a 0.8 eV Lorentzian broadening.

into the unoccupied 3*d* state, which is relatively unaffected by coordination and bond strength. On the other hand, in Zn^{2+} the 3*d* orbitals are occupied and the transitions are to the more diffuse 4*s* orbitals. Moreover, Zn^{2+} occupies a unique position within the structures of both Zn-substituted barlowite and herbertsmithite, allowing us to precisely compare the coordination environments of the interlayer sites between these two compounds. The measured Zn L-edge XANES spectra display good agreement with the simulated "interlayer Zn" spectra, as shown in Figure 6C and D. Just as in the Zn K-edge EXAFS data, the Zn L-edge XANES of $\mathbf{Zn}^{\mathrm{H}}_{0.56}$ (Figure S2B) and $\mathbf{Zn}^{\mathrm{H}}_{0.95}$ match well, indicating that their local coordinations are identical; this confirms that the Zn^{2+} occupies the same site in both compositions. Calculations were also performed for modified unit cells of idealized $\mathbf{Zn}_{0.95}$ and herbertsmithite with Zn^{2+} placed

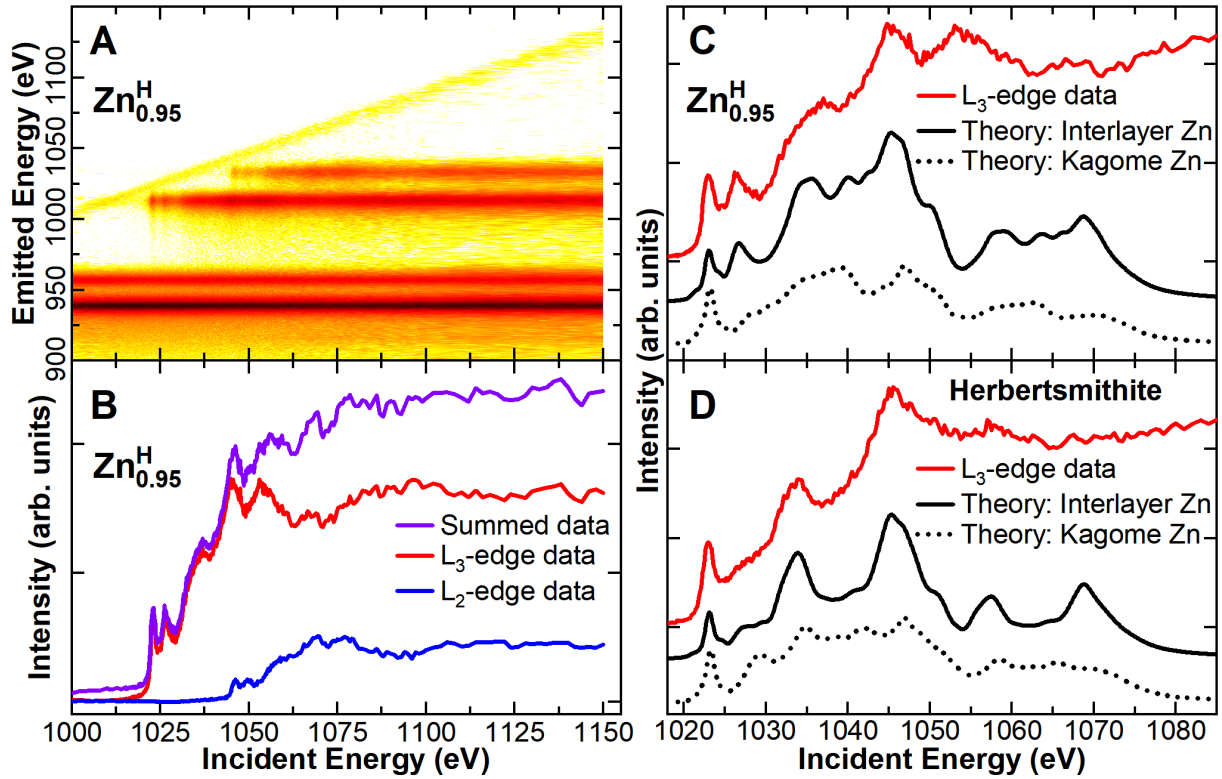

FIG. 6. A) Zn L-edge RIXS plane of $\mathbf{Zn}^{\mathrm{H}}_{0.95}$ showing the L-α fluorescence with emitted energy of 1012 eV and the L-β fluorescence with emitted energy of 1035 eV, corresponding to the L_3 and L_2 edges, respectively. Fluorescence from the Cu L-α and L-β lines are visible between 920 and 960 eV, and the elastic scattering is visible as a diagonal line. A log scale has been used on the color map to emphasize the faint elastic line. B) Zn L-edge XANES data of $\mathbf{Zn}^{\mathrm{H}}_{0.95}$ measured at $T = 300$ K. The TES detector allows the L_2-edge and L_3-edge data to be separated; they are shown along with the summed data. C) and D) Zn L_3-edge XANES data of $\mathbf{Zn}^{\mathrm{H}}_{0.95}$ and herbertsmithite measured at $T = 300$ K, along with simulations based on the experimentally determined crystal structure ("interlayer Zn") and simulations where Zn occupies one of the kagome sites while Cu occupies the respective interlayer site in each structure ("kagome Zn"; see discussion in text). In C) and D), vertical offsets have been applied to separate the spectra. The calculated Zn spectra were broadened by convolution with a 0.8 eV Gaussian broadening, and the non-excitonic portion had an additional 0.8 eV Lorentzian broadening.

onto a kagome site and Cu^{2+} placed onto the interlayer site; this model is referred to as "kagome Zn" in Figure 6. These simulated spectra deviate significantly from the experimental spectra and the "interlayer Zn" models. The mismatch between the experimental data and "kagome Zn" model for $\mathbf{Zn}^{\mathrm{H}}_{0.95}$ (Figure 6C) is particularly visible in the 1025–1030 eV region, where the "kagome Zn" spectrum is missing a peak that is clearly present in the experimental data. The mismatch is reversed in the herbertsmithite spectra (Figure 6D), where the "kagome Zn" simulated spectrum has more of a peak in this region than the experimental spectrum. These simulations illustrate that no significant amount of antisite (Zn-on-kagome) disorder occurs in Zn-substituted barlowite and herbertsmithite.

Moreover, the free energies of the relaxed "kagome Zn" structures are significantly less stable than those of the relaxed "interlayer Zn" structures. For herbertsmithite, the "interlayer Zn" model is more stable than the "kagome Zn" model by 0.25 eV per Zn, while for Zn-barlowite the "interlayer Zn" model is more stable by 0.44 eV per Zn. This provides a thermodynamic rationale which further confirms that it is highly unlikely that Zn^{2+} cations substitute onto the kagome lattice. Additionally, the difference between the compounds suggests that Zn-barlowite is more stable than herbertsmithite and less susceptible to Zn-on-kagome antisite disorder.

While the Zn L-edge XANES spectra of all samples have a strong peak at ≈1023 eV, both Zn-barlowites ($\mathbf{Zn}^{\mathrm{H}}_{0.95}$ and $\mathbf{Zn}^{\mathrm{H}}_{0.56}$ in Figures 6A–C and S2B) have a second strong peak at ≈1026.5 eV that is significantly suppressed in the herbertsmithite spectra (Figure 6D). These data illustrate a fundamental difference in the interlayer Zn^{2+}'s local coordination between Zn-substituted barlowite and herbertsmithite, as illustrated in Figure 4. While both have six equivalent Zn–O bonds where the O's form two equilateral triangles above and below the Zn, in herbertsmithite the two triangles are staggered, while in Zn-barlowite the triangles are eclipsed. Thus, the local environment of Zn^{2+} in herbertsmithite is pseudo-octahedral and has inversion symmetry (point group D_{3d}).[26] Conversely, the Zn^{2+} in Zn-barlowite has

trigonal prismatic local coordination (point group D_{3h}), with a loss of inversion symmetry. While this coordination for Zn^{2+} is rare, it is not unprecedented; in a statistical survey of oxides, trigonal prismatic local coordination was found in 1.23% of Zn sites.[64] Calculated electron density isosurfaces confirm that both Zn-barlowite and herbertsmithite have peaks at ≈1023 eV but differ substantially at the energy of the peak observed only in Zn-barlowite (≈1026.5 eV; see Figure S6). To check if this effect is systematic, we performed analogous Zn L-edge measurements and simulations on materials with similar Zn^{2+} coordination environments (pseudo-octahedral rutile ZnF_2 and trigonal prismatic Sr_3ZnRhO_6);[65] as shown in Figures S7–S9, they exhibit similar spectra to herbertsmithite and Zn-barlowite, respectively. Thus, the simple one-peak spectrum appears to be characteristic of 6-coordinate Zn^{2+} with a locally cubic or pseudo-cubic/pseudo-octahedral environment, and the second prominent peak observed in Zn-barlowite results from the trigonal prismatic coordination and the subsequent loss of inversion symmetry.

IV. DISCUSSION AND CONCLUSION

In this work, we investigate several outstanding questions about the structure and possible site-mixing disorder in Zn-substituted barlowite and compare it to the best known kagome QSL candidate material, herbertsmithite. We first probe the likelihood of any Zn^{2+} substituting onto the kagome site, as it is desirable for the lattice to be as ideal and undistorted as possible. This question cannot be answered using standard crystallographic techniques (X-ray diffraction and powder neutron diffraction) due to the nearly identical scattering factors of Cu and Zn. Our experiments performed on multiple length scales show that both compositions of Zn-barlowite ($\mathbf{Zn}^{\mathrm{D}}_{0.95}$ and $\mathbf{Zn}^{\mathrm{H}}_{0.56}$) have ideal, fully occupied kagome layers of Cu^{2+} cations, as does herbertsmithite.[17] Fits to EXAFS data show no indications that Zn should occupy the kagome site but cannot definitively exclude this possibility. Single crystal anomalous diffraction allows us to determine that in the long-range structure no measurable amount of Zn^{2+} occupies the kagome site. First-principles simulations and experimental XANES data, which probe the local structure, further confirm that it is energetically unfavorable for Zn^{2+} to occupy a kagome site in both Zn-barlowite and herbertsmithite, and simulated models with Zn^{2+} on the kagome site are not consistent with the data. This provides strong evidence supporting our claim that Zn-substituted barlowite with $x \gtrsim 0.5$ is a viable QSL candidate,[28] which has also been supported by a recent μSR study.[66]

Next, we are able to make site assignments for the two distinct interlayer sites observed in both compositions of Zn-substituted barlowite—$x \approx 0.5$ ($\mathbf{Zn}^{\mathrm{D}}_{0.52}$ and $\mathbf{Zn}^{\mathrm{H}}_{0.56}$) and $x = 0.95$, as elucidated by ICP-AES—by SCXRD measurements in this and previous work.[28] As shown in Figure 4, one site lies at the center of the trigonal prismatic coordination environment, and the second lies off-center—matching the sites seen in the barlowite parent compound. The relative occupancies of these two sites, as measured by SCXRD and PXRD, differ as the composition changes. As the amount of Zn substitution increases, the occupancy of the centered site increases, suggesting that it is occupied by Zn^{2+}. This is consistent with predictions from Jahn-Teller theory, but these standard crystallographic measurements cannot, however, provide direct evidence for which sites Zn and Cu occupy in the structure. We use X-ray anomalous diffraction to show that Zn^{2+} occupies the centered interlayer site while Cu^{2+} occupies the kagome and off-center interlayer sites. Two sites are observed even for the single crystal found in the bulk $\mathbf{Zn}^{\mathrm{D}}_{0.95}$ sample, which is likely not representative of the bulk and whose occupancies for the centered and off-center sites are 0.85 and 0.15, respectively. This conclusion is supported by the nearly identical Zn L-edge XANES spectra (which reflect the local structure) of $\mathbf{Zn}^{\mathrm{H}}_{0.56}$ and $\mathbf{Zn}^{\mathrm{H}}_{0.95}$, implying that Zn^{2+} must occupy the same site in both compositions of Zn-substituted barlowite.

However, herbertsmithite contains one interlayer site occupied by a mixture of both Zn^{2+} and Cu^{2+}.[17] The composition of the typical herbertsmithite crystal mirrors that of the $\mathbf{Zn}^{\mathrm{D}}_{0.95}$ crystal, but its site splitting behavior has never been observed in herbertsmithite. This points to a fundamental difference in the interlayer motifs between the two compounds.

In particular, we explore differences in the interlayer Zn^{2+} coordination between Zn-substituted barlowite and herbertsmithite, showing that they are nearly indistinguishable on one length scale but strikingly distinct when considered at other length scales. Their similarity on a local scale is exemplified by the near equivalence of their Zn K-edge EXAFS spectra (Figure 2C), which occurs because Zn^{2+} in both compounds occupies a centered site with six equivalent Zn–O bonds. However, on a slightly longer—but still local—length scale the differences between these structures become apparent. A combination of high-resolution XANES measurements and first-principles simulations reveal a handle for distinguishing (pseudo-)octahedral and trigonal prismatic Zn^{2+} coordination environments by the number of peaks close to the edge jump, and this trend is borne out by experimental data and calculations of other materials that share these Zn^{2+} coordination environments.

Taken together, our observations suggest that Zn-barlowite is less disordered than herbertsmithite due to its unique interlayer site splitting (mixed occupancy is not observed on either interlayer site). This may also allow it to support a higher amount of Zn substitution, thus facilitating more optimal low-energy measurements of its likely QSL ground state. Such measurements in herbertsmithite single crystal samples are made difficult due to the presence of magnetic Cu^{2+} "impurities" be-

tween the kagome layers.[16] Such detailed neutron scattering measurements require deuterated single crystals, which we report here for the first time. Additionally, the significant difference between the two QSL candidates in the free energies of the "kagome Zn" and "interlayer Zn" models suggests that Zn-substituted barlowite is more thermodynamically stable than herbertsmithite, so large crystals may be grown with the highest levels of Zn-substitution. This is consistent with previous first-principles calculations[34]. Interestingly, the similarity of the bulk magnetic susceptibility of Zn-barlowite and herbertsmithite, in spite of the measured differences in the local structure around the interlayer defects, indicates that the kagome QSL is robust to this type of disorder.[28] Hence, Zn-substituted barlowite, as a QSL candidate, has the potential to further advance the experimental realization of this exotic phase of matter.

V. DATA AND MATERIALS AVAILABILITY

The data that supports the findings of this study is available from the corresponding authors upon reasonable request. Crystallographic Information Files (CIFs) have been deposited in the Cambridge Crystallographic Data Center (CCDC): 1899246, 1899248, 1995564.

[1] L. Balents, Spin liquids in frustrated magnets, Nature **464**, 199 (2010).

[2] P. W. Anderson, Resonating Valence Bonds: A New Kind of Insulator?, Mater. Res. Bull. **8**, 153 (1973).

[3] P. W. Anderson, The Resonating Valence Bond State in La_2CuO_4 and Superconductivity, Science **235**, 1196 (1987).

[4] M. P. Shores, E. A. Nytko, B. M. Bartlett, and D. G. Nocera, A Structurally Perfect $S = \frac{1}{2}$ Kagomé Antiferromagnet, J. Am. Chem. Soc. **127**, 13462 (2005).

[5] S. Sachdev, Kagomé- and triangular-lattice Heisenberg antiferromagnets: Ordering from quantum fluctuations and quantum-disordered ground states with unconfined bosonic spinons, Phys. Rev. B **45**, 12377 (1992).

[6] Y. Ran, M. Hermele, P. A. Lee, and X.-G. Wen, Projected-wave-function study of the spin-1/2 heisenberg model on the kagomé lattice, Phys. Rev. Lett. **98**, 117205 (2007).

[7] M. Hermele, Y. Ran, P. A. Lee, and X.-G. Wen, Properties of an algebraic spin liquid on the kagome lattice, Phys. Rev. B **77**, 224413 (2008).

[8] H. C. Jiang, Z. Y. Weng, and D. N. Sheng, Density Matrix Renormalization Group Numerical Study of the Kagome Antiferromagnet, Phys. Rev. Lett. **101**, 117203 (2008).

[9] S. Yan, D. A. Huse, and S. R. White, Spin-Liquid Ground State of the $S = \frac{1}{2}$ Kagome Heisenberg Antiferromagnet, Science **332**, 1173 (2011).

[10] S. Depenbrock, I. P. McCulloch, and U. Schollwöck, Nature of the Spin-Liquid Ground State of the $S = \frac{1}{2}$ Heisenberg Model on the Kagome Lattice, Phys. Rev. Lett. **109**, 067201 (2012).

[11] Z. Hao and O. Tchernyshyov, Spin-$\frac{1}{2}$ Heisenberg antiferromagnet on the kagome lattice: Z_2 spin liquid with fermionic spinons, Phys. Rev. B **87**, 214404 (2013).

[12] Y.-C. He, M. P. Zaletel, M. Oshikawa, and F. Pollmann, Signatures of Dirac Cones in a DMRG Study of the Kagome Heisenberg Model, Phys. Rev. X **7**, 031020 (2017).

[13] R. S. W. Braithwaite, K. Mereiter, W. H. Paar, and A. M. Clark, Herbertsmithite, $Cu_3Zn(OH)_6Cl_2$, a new species, and the definition of paratacamite, Mineral. Mag. **68**, 527 (2004).

[14] T.-H. Han, J. S. Helton, S. Chu, D. G. Nocera, J. A. Rodriguez-Rivera, C. Broholm, and Y. S. Lee, Fractionalized excitations in the spin-liquid state of a kagome-lattice antiferromagnet., Nature **492**, 406 (2012).

[15] M. Fu, T. Imai, T.-H. Han, and Y. S. Lee, Evidence for a gapped spin-liquid ground state in a kagome Heisenberg antiferromagnet, Science **350**, 655 (2015).

[16] T.-H. Han, M. R. Norman, J.-J. Wen, J. A. Rodriguez-Rivera, J. S. Helton, C. Broholm, and Y. S. Lee, Correlated impurities and intrinsic spin-liquid physics in the kagome material herbertsmithite, Phys. Rev. B **94**, 060409(R) (2016).

[17] D. E. Freedman, T. H. Han, A. Prodi, P. Müller, Q.-Z. Huang, Y.-S. Chen, S. M. Webb, Y. S. Lee, T. M. McQueen, and D. G. Nocera, Site Specific X-Ray Anomalous Dispersion of the Geometrically Frustrated Kagomé Magnet, Herbertsmithite, $ZnCu_3(OH)_6Cl_2$, J. Am. Chem. Soc. **132**, 16185 (2010).

[18] P. Elliott, M. A. Cooper, and A. Pring, Barlowite, $Cu_4(OH)_6FBr$, a new mineral isotructural with claringbullite: description and crystal structure, Mineral. Mag. **78**, 1755 (2014).

[19] T.-H. Han, J. Singleton, and J. A. Schlueter, Barlowite: A Spin-$\frac{1}{2}$ Antiferromagnet With a Geometrically Perfect Kagome Motif, Phys. Rev. Lett. **113**, 227203 (2014).

[20] H. O. Jeschke, F. Salvat-Pujol, E. Gati, N. H. Hoang, B. Wolf, M. Lang, J. A. Schlueter, and R. Valentí, Barlowite as a canted antiferromagnet: Theory and experiment, Phys. Rev. B **92**, 094417 (2015).

[21] T.-H. Han, E. D. Isaacs, J. A. Schlueter, and J. Singleton, Anisotropy: Spin order and magnetization of single-crystalline $Cu_4(OH)_6FBr$ barlowite, Phys. Rev. B **93**, 214416 (2016).

[22] K. Tustain, G. J. Nilsen, C. Ritter, I. da Silva, and L. Clark, Nuclear and magnetic structures of the frustrated quantum antiferromagnet barlowite, $Cu_4(OH)_6FBr$, Phys. Rev. Mater. **2**, 111405(R) (2018).

[23] C. M. Pasco, B. A. Trump, T. T. Tran, Z. A. Kelly, C. Hoffmann, I. Heinmaa, R. Stern, and T. M. McQueen, Single-crystal growth of $Cu_4(OH)_6BrF$ and universal behavior in quantum spin liquid candidates synthetic barlowite and herbertsmithite, Phys. Rev. Mater. **2**, 044406 (2018).

[24] R. W. Smaha, W. He, J. P. Sheckelton, J. Wen, and Y. S. Lee, Synthesis-dependent properties of barlowite and Zn-substituted barlowite, J. Solid State Chem. **268**, 123 (2018).

[25] A. Henderson, L. Dong, S. Biswas, H. I. Revell, Y. Xin, R. Valenti, A. Schlueter, and T. Siegrist, Order–disorder transition in the $S = \frac{1}{2}$ kagome antiferromagnets claringbullite and barlowite, Chem. Commun. **55**, 11587 (2019).

[26] J. Echeverría, E. Cremades, A. J. Amoroso, and S. Alvarez, Jahn-Teller distortions of six-coordinate Cu^{II} compounds: *cis* or *trans*?, Chem. Commun. , 4242 (2009).

[27] P. C. Burns, M. A. Cooper, and F. C. Hawthorne, Claringbullite: A Cu^{2+} Oxysalt With Cu^{2+} in Trigonal-Prismatic Coordination, Can. Mineral. **33**, 633 (1995).

[28] R. W. Smaha, W. He, J. M. Jiang, J. Wen, Y. F. Jiang, J. P. Sheckelton, C. J. Titus, S. G. Wang, Y. S. Chen, S. J. Teat, A. A. Aczel, Y. Zhao, G. Xu, J. W. Lynn, H. C. Jiang, and Y. S. Lee, Materializing rival ground states in the barlowite family of kagome magnets: quantum spin liquid, spin ordered, and valence bond crystal states, npj Quantum Mater. **5**, 23 (2020).

[29] A. Zorko, M. Herak, M. Gomilšek, J. van Tol, M. Velázquez, P. Khuntia, F. Bert, and P. Mendels, Symmetry Reduction in the Quantum Kagome Antiferromagnet Herbertsmithite, Phys. Rev. Lett. **118**, 017202 (2017).

[30] N. J. Laurita, A. Ron, J. W. Han, A. Scheie, J. P. Sheckelton, R. W. Smaha, W. He, J. J. Wen, J. S. Lee, Y. S. Lee, M. R. Norman, and D. Hsieh, Evidence for a Parity Broken Monoclinic Ground State in the S = $\frac{1}{2}$ Kagomé Antiferromagnet Herbertsmithite (2019), arXiv:1910.13606 [cond-mat.str-el].

[31] P. Khuntia, M. Velazquez, Q. Barthélemy, F. Bert, E. Kermarrec, A. Legros, B. Bernu, L. Messio, A. Zorko, and P. Mendels, Gapless ground state in the archetypal quantum kagome antiferromagnet $ZnCu_3(OH)_6Cl_2$, Nat. Phys. **16**, 469 (2020).

[32] M. R. Norman, N. J. Laurita, and D. Hsieh, Valence bond phases of herbertsmithite and related copper kagome materials, Phys. Rev. Res. **2**, 013055 (2020).

[33] Y. Li, A. Pustogow, M. Bories, P. Puphal, C. Krellner, M. Dressel, and R. Valentí, Lattice dynamics in the spin-$\frac{1}{2}$ frustrated kagome compound herbertsmithite, Phys. Rev. B **101**, 161115(R) (2020).

[34] Z. Liu, X. Zou, J.-W. Mei, and F. Liu, Selectively doping barlowite for quantum spin liquid: A first-principles study, Phys. Rev. B **92**, 220102(R) (2015).

[35] D. Guterding, R. Valentí, and H. O. Jeschke, Reduction of magnetic interlayer coupling in barlowite through isoelectronic substitution, Phys. Rev. B **94**, 125136 (2016).

[36] Z. Feng, Z. Li, X. Meng, W. Yi, Y. Wei, J. Zhang, Y.-C. Wang, W. Jiang, Z. Liu, S. Li, F. Liu, J. Luo, S. Li, G.-q. Zheng, Z. Y. Meng, J.-W. Mei, and Y. Shi, Gapped Spin-$\frac{1}{2}$ Spinon Excitations in a New Kagome Quantum Spin Liquid Compound $Cu_3Zn(OH)_6FBr$, Chin. Phys. Lett. **34**, 077502 (2017).

[37] Z. Feng, Y. Wei, R. Liu, D. Yan, Y.-C. Wang, J. Luo, A. Senyshyn, C. Cruz, W. Yi, J.-W. Mei, Z. Y. Meng, Y. Shi, and S. Li, Effect of Zn doping on the antiferromagnetism in kagome $Cu_{4-x}Zn_x(OH)_6FBr$, Phys. Rev. B **98**, 155127 (2018).

[38] S.-J. Lee, C. J. Titus, R. Alonso Mori, M. L. Baker, D. A. Bennett, H.-M. Cho, W. B. Doriese, J. W. Fowler, K. J. Gaffney, A. Gallo, J. D. Gard, G. C. Hilton, H. Jang, Y. I. Joe, C. J. Kenney, J. Knight, T. Kroll, J.-S. Lee, D. Li, D. Lu, R. Marks, M. P. Minitti, K. M. Morgan, H. Ogasawara, G. C. O'Neil, C. D. Reintsema, D. R. Schmidt, D. Sokaras, J. N. Ullom, T.-C. Weng, C. Williams, B. A. Young, D. S. Swetz, K. D. Irwin, and D. Nordlund, Soft X-ray spectroscopy with transition-edge sensors at Stanford Synchrotron Radiation Lightsource beamline 10-1, Rev. Sci. Instrum. **90**, 113101 (2019).

[39] Vinson, J. and Rehr, J. J. and Kas, J. J. and Shirley, E. L., Bethe-Salpeter equation calculations of core excitation spectra, Phys. Rev. B **83**, 115106 (2011).

[40] T. H. Han, J. S. Helton, S. Chu, A. Prodi, D. K. Singh, C. Mazzoli, P. Müller, D. G. Nocera, and Y. S. Lee, Synthesis and characterization of single crystals of the spin-$\frac{1}{2}$ kagome-lattice antiferromagnets $Zn_xCu_{4-x}(OH)_6Cl_2$, Phys. Rev. B **83**, 100402(R) (2011).

[41] B. H. Toby and R. B. Von Dreele, *GSAS-II*: the genesis of a modern open-source all purpose crystallography software package, J. Appl. Crystallogr. **46**, 544 (2013).

[42] Bruker AXS Inc., Madison, Wisconsin (2016).

[43] G. M. Sheldrick, Crystal structure refinement with SHELXL, Acta Crystallogr. C **71**, 3 (2015).

[44] O. V. Dolomanov, L. J. Bourhis, R. J. Gildea, J. A. K. Howard, and H. Puschmann, *OLEX2*: A complete structure solution, refinement, and analysis program, J. Appl. Crystallogr. **42**, 339 (2009).

[45] S. Sasaki, Numerical Tables of Anomalous Scattering Factors Calculated by the Cromer and Liberman's Method, KEK Report **88-14** (1989).

[46] D. T. Cromer and D. Liberman, Relativistic Calculation of Anomalous Scattering Factors for X Rays, J. Chem. Phys. **53**, 1891 (1970).

[47] B. Ravel and M. Newville, *ATHENA*, *ARTEMIS*, *HEPHAESTUS*: data analysis for X-ray absorption spectroscopy using *IFEFFIT*, J. Synchrotron Radiat. **12**, 537 (2005).

[48] J. J. Rehr, J. Mustre de Leon, S. I. Zabinsky, and R. C. Albers, Theoretical X-Ray Absorption Fine Structure Standards, J. Am. Chem. Soc. **113**, 5135 (1991).

[49] G. Kresse and J. Hafner, *Ab initio* molecular dynamics for liquid metals, Phys. Rev. B **47**, 558 (1993).

[50] G. Kresse and J. Hafner, *Ab initio* molecular-dynamics simulation of the liquid-metal–amorphous-semiconductor transition in germanium, Phys. Rev. B **49**, 14251 (1994).

[51] G. Kresse and J. Furthmüller, Efficiency of ab-initio total energy calculations for metals and semiconductors using a plane-wave basis set, Comp. Mater. Sci. **6**, 15 (1996).

[52] G. Kresse and J. Furthmüller, Efficient iterative schemes for *ab initio* total-energy calculations using a plane-wave basis set, Phys. Rev. B **54**, 11169 (1996).

[53] G. I. Csonka, J. P. Perdew, A. Ruzsinszky, P. H. T. Philipsen, S. Lebègue, J. Paier, O. A. Vydrov, and J. G. Ángyán, Assessing the performance of recent density functionals for bulk solids, Phys. Rev. B **79**, 155107 (2009).

[54] K. Gilmore, J. Vinson, E. Shirley, D. Prendergast, C. Pemmaraju, J. Kas, F. Vila, and J. Rehr, Efficient implementation of core-excitation bethe–salpeter equation calculations, Comp. Phys. Commun. **197**, 109 (2015).

[55] P. Giannozzi, S. Baroni, N. Bonini, M. Calandra, R. Car, C. Cavazzoni, D. Ceresoli, G. L. Chiarotti, M. Cococcioni, I. Dabo, A. D. Corso, S. de Gironcoli, S. Fabris, G. Fratesi, R. Gebauer, U. Gerstmann, C. Gougoussis, A. Kokalj, M. Lazzeri, L. Martin-Samos, N. Marzari, F. Mauri, R. Mazzarello, S. Paolini, A. Pasquarello, L. Paulatto, C. Sbraccia, S. Scandolo, G. Sclauzero, A. P. Seitsonen, A. Smogunov, P. Umari, and R. M. Wentzcovitch, QUANTUM ESPRESSO: a modular and open-

source software project for quantum simulations of materials, J. Phys. Condens. Matter **21**, 395502 (2009).
[56] See Supplemental Material at [URL] for additional details about the crystallography, EXAFS fits, anomalous diffraction measurements, OCEAN calculations, and XANES spectra.
[57] M. Newville, Fundamentals of XAFS, Rev. Mineral. Geochem. **78**, 33 (2014).
[58] K. Momma and F. Izumi, *VESTA 3* for three-dimensional visualization of crystal, volumetric and morphology data, J. Appl. Crystallogr. **44**, 1272 (2011).
[59] S. Chu, P. Müller, D. G. Nocera, and Y. S. Lee, Hydrothermal growth of single crystals of the quantum magnets: Clinoatacamite, paratacamite, and herbertsmithite, Appl. Phys. Lett. **98**, 092508 (2011).
[60] M. D. Welch, M. J. Sciberras, P. A. Williams, P. Leverett, J. Schlüter, and T. Malcherek, A temperature-induced reversible transformation between paratacamite and herbertsmithite, Phys. Chem. Miner. **41**, 33 (2014).
[61] H. O. Jeschke, F. Salvat-Pujol, and R. Valentí, First-principles determination of Heisenberg Hamiltonian parameters for the spin-$\frac{1}{2}$ kagome antiferromagnet $ZnCu_3(OH)_6Cl_2$, Phys. Rev. B **88**, 075106 (2013).
[62] Q. Liu, Q. Yao, Z. A. Kelly, C. M. Pasco, T. M. McQueen, S. Lany, and A. Zunger, Electron Doping of Proposed Kagome Quantum Spin Liquid Produces Localized States in the Band Gap, Phys. Rev. Lett. **121**, 186402 (2018).
[63] W. Jiang, H. Huang, J. W. Mei, and F. Liu, Li doped kagome spin liquid compounds, Phys. Chem. Chem. Phys. **20**, 21693 (2018).
[64] D. Waroquiers, X. Gonze, G.-M. Rignanese, C. Welker-Nieuwoudt, F. Rosowski, M. Göbel, S. Schenk, P. Degelmann, R. André, R. Glaum, and G. Hautier, Statistical analysis of coordination environments in oxides, Chem. Mater. **29**, 8346 (2017).
[65] R. Layland and H. zur Loye, Synthesis, characterization, and magnetic properties of a commensurate and incommensurate phase of Sr_3ZnRhO_6: zinc in trigonal prismatic coordination, J. Alloys Compd. **299**, 118 (2000).
[66] K. Tustain, B. Ward-O'Brien, F. Bert, T. Han, H. Luetkens, T. Lancaster, B. M. Huddart, P. J. Baker, and L. Clark, From magnetic order to quantum disorder in the Zn-barlowite series of $S = 1/2$ kagomé antiferromagnets, npj Quantum Mater. **5**, 74 (2020).
[67] S. J. George, M. D. Lowery, E. I. Solomon, and S. P. Cramer, Copper L-Edge Spectral Studies: A Direct Experimental Probe of the Ground-State Covalency in the Blue Copper Site in Plastocyanin, J. Am. Chem. Soc. **115**, 2968 (1993).
[68] I. M. Dimucci, J. T. Lukens, S. Chatterjee, K. M. Carsch, C. J. Titus, S. J. Lee, D. Nordlund, T. A. Betley, S. N. MacMillan, and K. M. Lancaster, The Myth of d^8 Copper(III), J. Am. Chem. Soc. **141**, 18508 (2019).
[69] A. Jain, S. P. Ong, G. Hautier, W. Chen, W. D. Richards, S. Dacek, S. Cholia, D. Gunter, D. Skinner, G. Ceder, and K. A. Persson, Commentary: The Materials Project: A materials genome approach to accelerating materials innovation, APL Mater. **1**, 011002 (2013).

ACKNOWLEDGMENTS

The authors would like to thank S. Conradson and L.B. Gee for helpful discussions relating to EXAFS and S. Lapidus for assistance at APS beamline 11-BM. The work at Stanford and SLAC was supported by the U.S. Department of Energy (DOE), Office of Science, Basic Energy Sciences (BES), Materials Sciences and Engineering Division, under Contract No. DE-AC02-76SF00515. The experimental work was performed at the Stanford Institute for Materials and Energy Sciences (SIMES), and the computational work was performed at the Theory Institute for Materials and Energy Spectroscopies (TIMES). This research used resources of the Advanced Light Source, which is a DOE Office of Science User Facility under contract No. DE-AC02-05CH11231. Use of the Stanford Synchrotron Radiation Lightsource, SLAC National Accelerator Laboratory, is supported by the DOE, Office of Science, BES, under Contract No. DE-AC02-76SF00515. Use of the Advanced Photon Source, an Office of Science User Facility operated for the U.S. DOE Office of Science by Argonne National Laboratory, was supported by the U.S. DOE under Contract No. DE-AC02-06CH11357. NSF's ChemMatCARS Sector 15 is supported by the Divisions of Chemistry (CHE) and Materials Research (DMR), National Science Foundation, under grant number NSF/CHE-1834750. This research used resources of the National Energy Research Scientific Computing Center (NERSC), a DOE Office of Science User Facility operated under Contract No. DE-AC02-05CH11231. Part of this work was performed at the Stanford Nano Shared Facilities (SNSF), supported by the NSF under award ECCS-1542152. R.W.S. was supported by the Department of Defense (DoD) through the NDSEG Fellowship Program and by a NSF Graduate Research Fellowship (DGE-1656518). Certain commercial equipment, instruments, or materials are identified in this paper in order to specify the experimental procedure adequately. Such identification is not intended to imply recommendation or endorsement by NIST, nor is it intended to imply that the materials or equipment identified are necessarily the best available for the purpose.

VI. AUTHOR CONTRIBUTIONS

R.W.S. and Y.S.L. conceived the study, interpreted the data, and wrote the manuscript with contributions and comments from all authors. R.W.S. synthesized barlowite **2** and Zn-barlowite and performed and analyzed X-ray diffraction measurements. I.B. performed and analyzed simulations with C.D.P., J.T.V, and T.P.D. C.J.T. performed and analyzed EXAFS and XANES measurements. J.M.J. performed and analyzed anomalous diffraction measurements. J.P.S. and W.H. synthesized herbertsmithite and barlowite **1**, respectively. S.G.W., Y.-S.C., and S.J.T aided at beamtimes.

Supplemental Material for: Site-Specific Structure at Multiple Length Scales in Kagome Quantum Spin Liquid Candidates

Rebecca W. Smaha,[1,2,*] Idris Boukahil,[3,4,†] Charles J. Titus,[3,†] Jack Mingde Jiang,[1,5,†] John P. Sheckelton,[1] Wei He,[1,6] Jiajia Wen,[1] John Vinson,[7] Suyin Grass Wang,[8] Yu-Sheng Chen,[8] Simon J. Teat,[9] Thomas P. Devereaux,[1,6] C. Das Pemmaraju,[4] and Young S. Lee[1,5,‡]

[1]*Stanford Institute for Materials and Energy Sciences, SLAC National Accelerator Laboratory, Menlo Park, California 94025, USA*
[2]*Department of Chemistry, Stanford University, Stanford, California 94305, USA*
[3]*Department of Physics, Stanford University, Stanford, California 94305, USA*
[4]*Theory Institute for Materials and Energy Spectroscopies, SLAC National Accelerator Laboratory, Menlo Park, California 94025, USA*
[5]*Department of Applied Physics, Stanford University, Stanford, California 94305, USA*
[6]*Department of Materials Science and Engineering, Stanford University, Stanford, California 94305, USA*
[7]*Material Measurement Laboratory, National Institute of Standards and Technology, 100 Bureau Drive, Gaithersburg, MD 20899*
[8]*NSF's ChemMatCARS, Center for Advanced Radiation Sources, c/o Advanced Photon Source/ANL, The University of Chicago, Argonne, Illinois 60439, USA*
[9]*Advanced Light Source, Lawrence Berkeley National Laboratory, Berkeley, California 94720, USA*

CONTENTS

* rsmaha@stanford.edu
† These authors contributed equally to this work
‡ youngsl@stanford.edu

I. CRYSTALLOGRAPHY OF $\mathbf{ZN}^{\mathrm{D}}_{0.52}$

We report here the first crystal structure of deuterated single crystalline Zn-substituted barlowite with no magnetic order. Low-temperature synchrotron powder and single crystal X-ray diffraction (PXRD and SCXRD) measurements were performed on Zn-substituted barlowite $\mathbf{Zn}^{\mathrm{D}}_{0.52}$, and PXRD was also performed at $T = 295$ K. The details of the SCXRD measurement are in Table S1. Crystallographic information from SCXRD is tabulated in Tables S2–S3, and crystallographic information from PXRD is tabulated in Table S4. Selected bond angles and distances are found in Tables S5–S6. The errors are statistical uncertainties computed by the respective least-squares refinement programs: SHELXTL and OLEX2 for SCXRD and GSAS-II for PXRD.[1–3]

Slight variations in the site occupancies of the two interlayer sites—centered (point group D_{3h}) and the set of three off-center (point group C_{2v}) sites observed in all-Cu barlowite—occur across the different measurement techniques and temperatures. The following discussion assumes that the centered site is occupied by Zn^{2+} and the off-center sites are occupied by Cu^{2+}, as confirmed by the anomalous scattering measurements in this work. Rietveld refinements of PXRD data on the same sample of $\mathbf{Zn}^{\mathrm{D}}_{0.52}$ at different temperatures show slight variation in the relative occupancies of the interlayer sites, ranging from 51.5(6)% Zn and 48.6(6)% Cu at $T = 90$ K to 39.8(11)% Zn and 60.3(12)% Cu at $T = 295$ K. The SCXRD refinement yields 46(4)% Zn and 53.4(39)% Cu at $T = 100$ K. The average formula for $\mathbf{Zn}^{\mathrm{D}}_{0.52}$ from all diffraction measurements is $Cu_{3.54}Zn_{0.46}(OH)_6FBr$, consistent with the ICP-AES results (52% Zn and 48% Cu on the interlayer).

TABLE S1: Single crystal data for Zn-substituted barlowite $\mathbf{Zn}^{\mathrm{D}}_{0.52}$

Empirical Formula	$Cu_{3.54}Zn_{0.46}(OD)_6FBr$
Temperature	100 K
Incident Radiation (Å)	0.7288
Formula Weight ($g \cdot mol^{-1}$)	461.68
Crystal System	Hexagonal
Space Group	$P6_3/mmc$
a (Å)	6.6635(3)
b (Å)	6.6635(3)
c (Å)	9.2835(5)
α (°)	90
β (°)	90
γ (°)	120
Volume ($Å^3$)	356.98(4)
Z	2
Density (calc.) ($g \cdot cm^3$)	4.295
Absorption Coeff. (mm^{-1})	18.708
$F(000)$	429.0
Crystal Size (mm^3)	$0.005 \times 0.005 \times 0.025$
θ range (°)	4.264–37.349
Index ranges	$-11 \leq h \leq 11, -11 \leq k \leq 10, -15 \leq l \leq 15$
Reflections coll./unique	10393/364
Completeness to θ_{max}	0.997
T_{min}, T_{max}	0.6251, 0.7473
R_{int}	0.0424
Goodness-of-fit on F^2	1.303
Data/parameters/restraints	364/26/1
Final R indices $[I>2\sigma(I)]$[a]	R_1=0.0188, wR_2=0.0406
R indices (all data)[a]	R_1=0.0191, wR_2=0.0407
$\Delta\rho_{max}$, $\Delta\rho_{min}$ ($e \cdot Å^{-3}$)	1.528, -0.831

[a] $R_1 = \sum ||F_o| - |F_c|| / \sum |F_o|$,
$wR_2 = [\sum w({F_o}^2 - {F_c}^2)^2 / \sum ({F_o}^2)^2]^{1/2}$

TABLE S2: Crystallographic data for $\mathbf{Zn}^{\mathrm{D}}_{0.52}$ from synchrotron SCXRD. U_{eq} is defined as 1/3 of the trace of the orthogonalized U_{IJ} tensor. The empirical formula is $Cu_{3.54}Zn_{0.46}(OD)_6FBr$

	Atom	**Wyckoff Position**	**x**	**y**	**z**	**U**$_{eq}$ (Å^2)	**Occ.**
$\mathbf{Zn}^{\mathrm{D}}_{0.52}$	Cu1	6*g*	0.5	0	0.5	0.00576(9)	1
100 K	Cu2	12*j*	0.7400(20)	0.3702(12)	0.25	0.0036(10)	0.178(13)
$P6_3/mmc$	Zn1	2*d*	0.66667	0.33333	0.25	0.0038(12)	0.46(4)
	Br1	2*c*	0.66667	0.33333	0.75	0.00587(10)	1
	F1	2*b*	1	0	0.25	0.0088(4)	1
	O1	12*k*	0.79796(9)	0.20204(9)	0.40763(11)	0.00574(19)	1
	D1	12*k*	0.8609(15)	0.1391(15)	0.3750(20)	0.009	1

TABLE S3: Anisotropic displacement parameters for $\mathbf{Zn}^{\mathrm{D}}_{0.52}$ from synchrotron SCXRD. The anisotropic displacement factor exponent takes the form: $-2\pi^2[h^2a^{*2}U_{11} + 2hka^*b^*U_{12} + ...]$

Atom	**U**$_{11}$ (Å^2)	**U**$_{22}$ (Å^2)	**U**$_{33}$ (Å^2)	**U**$_{23}$ (Å^2)	**U**$_{13}$ (Å^2)	**U**$_{12}$ (Å^2)
Cu1	0.00411(11)	0.0410(13)	0.00906(14)	0.00197(7)	0.00099(4)	0.00205(6)
Cu2	0.005(3)	0.0041(10)	0.0024(7)	0	0	0.0023(13)
Zn1	0.0040(18)	0.0040(18)	0.0035(5)	0	0	0.0020(9)
Br1	0.00653(12)	0.00653(12)	0.00457(15)	0	0	0.00326(6)
F1	0.0071(6)	0.0071(6)	0.0122(11)	0	0	0.0035(3)
O1	0.0053(3)	0.0053(3)	0.0069(4)	-0.00033(16)	0.00033(16)	0.0028(3)

TABLE S4: Crystallographic data for $\mathbf{Zn}^{\mathrm{D}}_{0.52}$ from Rietveld refinements of synchrotron PXRD data (λ = 0.412702 Å) in $P6_3/mmc$. The refined formula, not including D, is shown

	Atom	**Wyckoff Position**	**x**	**y**	**z**	**U_{iso}**	**Occ.**
$\mathbf{Zn}^{\mathrm{D}}_{0.52}$ [a]	Cu1	6*g*	0.5	0	0.5	0.00281(4)	1
T = 90 K	Zn1	2*d*	0.66667	0.33333	0.25	0.00350(32)	0.515(6)
a = 6.661426(9) Å	Cu2	6*h*	0.62930(90)	0.25854(180)	0.25	0.00281(4)	0.162(2)
c = 9.286484(8) Å	Br1	2*c*	0.66667	0.33333	0.75	0.00326(6)	1
V = 356.875(1) Å^3	F1	2*b*	1	0	0.75	0.00775(31)	1
$Cu_{3.48}Zn_{0.52}O_6FBr$	O1	12*k*	0.79869(7)	0.20131(7)	0.40679(9)	0.00246(16)	1
$\mathbf{Zn}^{\mathrm{D}}_{0.52}$ [b]	Cu1	6*g*	0.5	0	0.5	0.00834(5)	1
T = 295 K	Zn1	2*d*	0.66667	0.33333	0.25	0.00183(60)	0.398(11)
a = 6.672813(13) Å	Cu2	6*h*	0.63381(126)	0.26758(252)	0.25	0.00834(5)	0.201(4)
c = 9.309858(5) Å	Br1	2*c*	0.66667	0.33333	0.75	0.01330(9)	1
V = 358.998(1) Å^3	F1	2*b*	1	0	0.75	0.02198(43)	1
$Cu_{3.60}Zn_{0.40}O_6FBr$	O1	12*k*	0.79846(7)	0.20154(7)	0.40737(10)	0.00688(18)	1

[a] GOF = 2.27, wR = 9.85%. LiF impurity: 0.00907(29) wt.%.
[b] GOF = 1.90, wR = 9.07%. LiF impurity: 0.00766(36) wt.%.

TABLE S5: Selected bond angles relating to the kagome Cu's extracted from SCXRD refinements and Rietveld refinements of PXRD data of $\mathbf{Zn}^{\mathrm{D}}_{0.52}$ in $P6_3/mmc$

Technique	SCXRD	PXRD	PXRD
Temperature	100 K	90 K	295 K
Cu1–O1–Cu1	117.01(5)°	116.43(4)°	116.70(5)°
Cu1–O1–Zn1	95.80(4)°	95.62(3)°	95.69(3)°
Cu1–O1–Cu2 (1)	107.1(4)°	107.11(3)°	105.71(3)°
Cu1–O1–Cu2 (2)	92.18(11)°	91.94(13)°	92.41(18)°
Cu1–O1–Cu2 (3)	88.8(3)°	88.59(12)°	89.53(17)°

TABLE S6: Selected bond distances in Å extracted from SCXRD refinements and Rietveld refinements of PXRD data of $\mathbf{Zn}^{\mathrm{D}}_{0.52}$ in $P6_3/mmc$

Technique	SCXRD	PXRD	PXRD
Temperature	100 K	90 K	295 K
Cu1–Cu1	3.33175(16)	3.33071(0)	3.33641(0)
Cu1–O1	1.9537(6)	1.9591(4)	1.9597(6)
Cu1–Br1	3.01441(12)	3.01460(0)	3.02120(0)
Zn1–O1	2.1065(11)	2.1072(7)	2.1135(8)
Cu2–O1 (1)	1.993(3)	1.992(5)	2.008(6)
Cu2–O1 (2)	1.993(3)	1.992(5)	2.008(6)
Cu2–O1 (3)	2.421(11)	2.4376(6)	2.4017(7)
Cu2–Cu2	0.74(2)	0.74775(0)	0.65794(0)
Cu1–Cu2 (1)	2.764(7)	2.75932(0)	2.79437(0)
Cu1–Cu2 (2)	3.176(5)	3.179(4)	3.163(5)
Cu1–Cu2 (3)	3.174(10)	3.179(4)	3.163(5)
Cu1–Zn1	3.01441(12)	3.01460(0)	3.02120(0)

II. EXAFS FITS

The real part of $\chi(R)$ of the K-edge EXAFS data and fits are plotted in Figure S1, displaying good agreement. Details of the r-space fits to Cu and Zn K-edge EXAFS data are shown in Tables S7 and S8, respectively. They list the coordination number (N), disorder parameter (σ^2, the mean square displacement around the path length), input effective path length (R_{eff}), path shift from the input path (δr), and refined path length (R = $R_{eff} + \delta$r) for each path. E_0 is an alignment parameter that is constant for all paths within a sample; it corrects for the arbitrary position of the $k = 0$ point. The data were weighted by k^3 before being Fourier transformed to χ(R). The Cu EXAFS fits were performed in a k-range of 3–12.5 $Å^{-1}$ and an R-range of 1.1–4.4 Å. The Zn EXAFS fits were performed in a k-range of 3–13 $^{-1}$ and an R-range of 1.0–4.0 Å. All fits were performed in R-space using χ^2 minimization. Where possible, the number of free parameters was reduced by linking σ^2 values for paths of similar length and element. All refined path lengths are within 0.09 Å of the starting values. The errors are statistical uncertainties computed by the refinement program, Artemis.[4]

For the Cu EXAFS of $\mathbf{Zn}^{\mathrm{H}}_{0.95}$, a five-path model was used that included Cu–O (1.95 Å), Cu–Zn (2.99 Å), Cu–Br (3.01 Å), Cu–Cu (3.34 Å), and Cu–O (4.14 Å). For **1** and **2**, the Cu–Zn path was replaced by two Cu–Cu paths (2.85 Å and 3.15 Å) to capture the off-center Cu interlayer site. $\mathbf{Zn}^{\mathrm{H}}_{0.56}$ posed a challenge due to fractional occupation of the off-center interlayer sites by Cu, but it was fit well to a seven-path model that included both the Cu–Zn path from $\mathbf{Zn}^{\mathrm{H}}_{0.95}$ and the Cu–Cu paths from **1** and **2**, with path coordination numbers set according to the expected stoichiometry. For herbertsmithite, a seven-path model was used consisting of Cu–O (1.98 Å), Cu–Cl (2.77 Å), Cu–Zn (3.07 Å), Cu–Cu (3.45 Å), Cu–O (3.67 Å), Cu–O (3.89 Å), and Cu–O (4.22 Å). Several paths (such as the Cu–Br path for barlowite **1**, **2**, and $\mathbf{Zn}^{\mathrm{H}}_{0.56}$) were not included because they did not impact the goodness of fit enough to justify adding additional degrees of freedom. Multiple-scattering paths were similarly excluded.

For Zn EXAFS fits of $\mathbf{Zn}^{\mathrm{H}}_{0.56}$ and $\mathbf{Zn}^{\mathrm{H}}_{0.95}$, Zn–O (2.11 Å), Zn–Cu (3.02 Å), and Zn–Br (3.85 Å) paths were used. For herbertsmithite, Zn–O (2.11 Å), Zn–Cu (3.06 Å), Zn–Cl (3.96 Å), Zn–Cl (4.29 Å), and Zn–O (4.71 Å) paths were used.

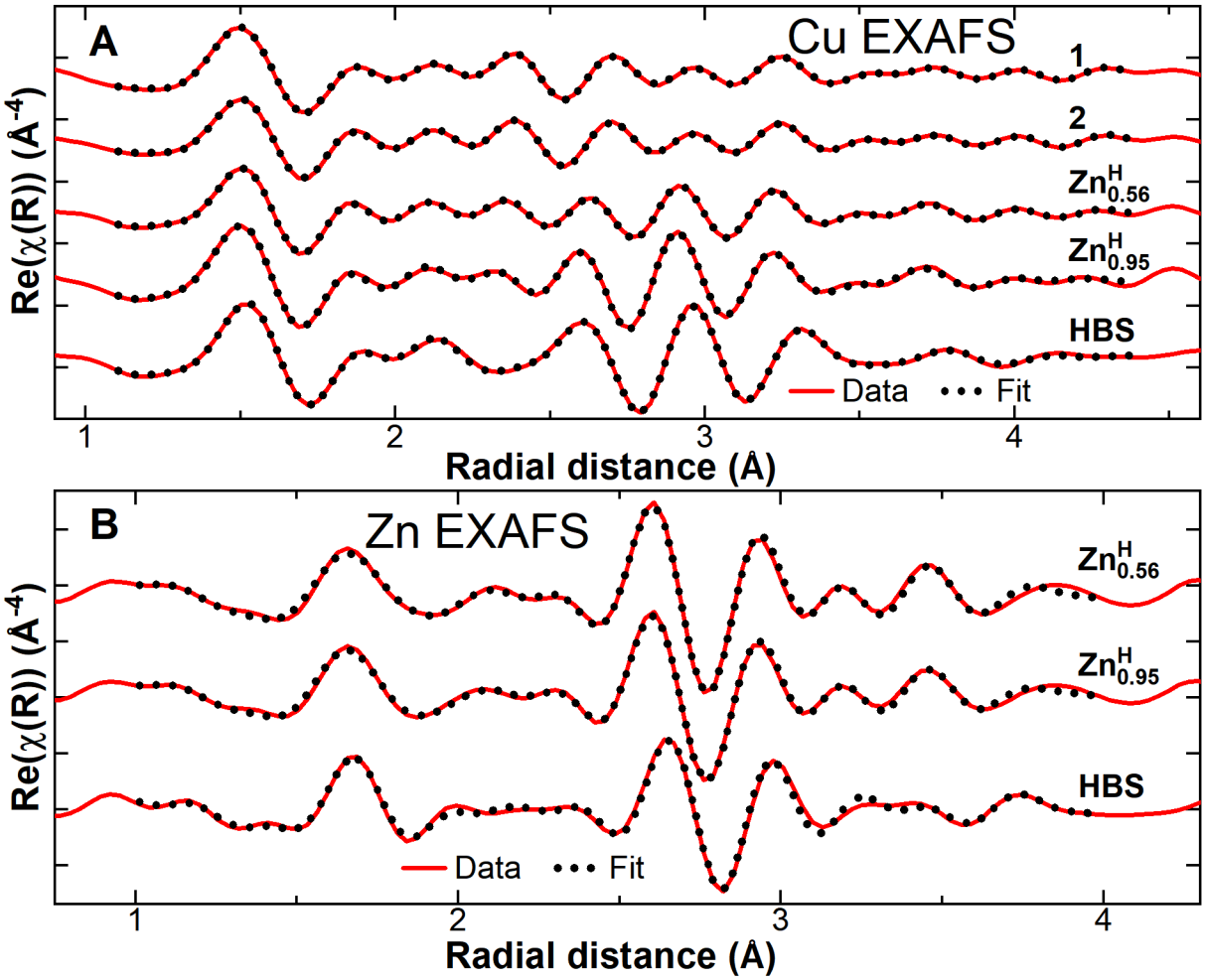

FIG. S1: A) Real part of $\chi(R)$ of the Cu K-edge EXAFS data and fits of barlowite **1**, barlowite **2**, $\mathbf{Zn}^{\mathrm{H}}_{0.56}$, $\mathbf{Zn}^{\mathrm{H}}_{0.95}$, and herbertsmithite measured at $T = 10$ K. C) Real part of $\chi(R)$ of the Zn K-edge EXAFS data and fits to $\mathbf{Zn}^{\mathrm{H}}_{0.56}$, $\mathbf{Zn}^{\mathrm{H}}_{0.95}$, and herbertsmithite measured at $T = 10$ K. Vertical offsets have been applied to separate the spectra.

TABLE S7: Cu EXAFS fit parameters and results

Sample	Path	N	σ^2 (Å^2)	E_0 (eV)	R_{eff} (Å)	δr (Å)	R (Å)
Barlowite 1	Cu–O	4	0.00412	4.863	1.94530	0.01063	1.95593
R-factor: 0.0026221	Cu–Cu	1	0.00297	4.863	2.81560	0.03072	2.84632
Reduced χ^2: 626.237	Cu–Cu	2	0.00616	4.863	3.13510	0.01396	3.14906
	Cu–Cu	3	0.00616	4.863	3.33680	0.01562	3.35242
	Cu–O	6	0.00882	4.863	4.15980	-0.00282	4.15698
	Cu–Cu	0.75	0.00212	4.863	4.48400	-0.05462	4.42938
Barlowite 2	Cu–O	4	0.00274	5.153	1.94530	0.01021	1.95551
R-factor: 0.0020536	Cu–Cu	1	0.00166	5.153	2.81560	0.02910	2.84470
Reduced χ^2: 499.730	Cu–Cu	2	0.00505	5.153	3.13510	0.01171	3.14681
	Cu–Cu	3	0.00505	5.153	3.33680	0.01422	3.35102
	Cu–O	6	0.00904	5.153	4.15980	0.00873	4.16852
	Cu–Cu	0.75	0.00112	5.153	4.48400	-0.05070	4.43330
Zn$^{\mathrm{H}}_{0.56}$	Cu–O	4	0.00258	5.090	1.94530	0.00921	1.95451
R-factor: 0.0018376	Cu–Cu	1	0.00413	5.090	2.81560	0.02829	2.84389
Reduced χ^2: 640.497	Cu–Zn	1	0.00090	5.090	3.02420	-0.01177	3.01243
	Cu–Cu	2	0.00413	5.090	3.13510	-0.01032	3.12478
	Cu–Cu	3	0.00413	5.090	3.33680	0.00872	3.34552
	Cu–O	6	0.00441	5.090	4.11740	0.02885	4.14626
	Cu–Cu	0.75	0.00441	5.090	4.48400	-0.06056	4.42344
Zn$^{\mathrm{H}}_{0.95}$	Cu–O	4	0.00393	4.471	1.97580	-0.02469	1.95111
R-factor: 0.0022042	Cu–Zn	2	0.00779	4.471	3.02420	-0.04305	2.98115
Reduced χ^2: 536.404	Cu–Br	2	0.00318	4.471	3.02420	-0.01395	3.01025
	Cu–Cu	4	0.00779	4.471	3.33800	0.00524	3.34324
	Cu–O	8	0.00797	4.471	4.16220	-0.03320	4.12900
Herbertsmithite	Cu–O	4	0.00431	5.042	1.98360	-0.00501	1.97859
R-factor: 0.0029378	Cu–Cl	2	0.00765	5.042	2.77190	-0.00120	2.77069
Reduced χ^2: 1014.289	Cu–Zn	2	0.00280	5.042	3.06230	0.00448	3.06678
	Cu–Cu	4	0.00605	5.042	3.41490	0.03540	3.45030
	Cu–O	2	0.00431	5.042	3.58510	0.08908	3.67418
	Cu–O	2	0.00431	5.042	3.85020	0.03807	3.88827
	Cu–O	4	0.00431	5.042	4.28230	-0.06073	4.22157

TABLE S8: Zn EXAFS fit parameters and results

Sample	Path	N	σ^2 (Å^2)	E_0 (eV)	R_{eff} (Å)	δr (Å)	R (Å)
$\mathbf{Zn}^{\mathrm{H}}_{0.56}$	Zn–O	6	0.01036	1.972	2.10760	-0.01022	2.09738
R-factor: 0.0119578	Zn–Cu	6	0.00468	1.972	3.02420	0.00676	3.03096
Reduced χ^2: 317.810	Zn–Br	3	0.00564	1.972	3.85430	-0.02589	3.82841
$\mathbf{Zn}^{\mathrm{H}}_{0.95}$	Zn–O	6	0.00770	2.311	2.10760	-0.01655	2.09105
R-factor: 0.0111015	Zn–Cu	6	0.00414	2.311	3.02420	0.00668	3.03088
Reduced χ^2: 262.365	Zn–Br	3	0.00575	2.311	3.85430	-0.02262	3.83168
Herbertsmithite	Zn–O	6	0.00394	2.541	2.11220	-0.01478	2.09742
R-factor: 0.0161352	Zn–Cu	6	0.00284	2.541	3.06230	0.01512	3.07742
Reduced χ^2: 672.786	Zn–Cl	6	0.00987	2.541	3.96280	-0.01925	3.943558
	Zn–Cl	2	0.00219	2.541	4.29160	0.05384	4.34544
	Zn–O	12	0.00316	2.541	4.70770	0.01870	4.72640

III. ANOMALOUS DIFFRACTION

The wavelengths used for collecting anomalous diffraction data of $\mathbf{Zn}^{\mathrm{H}}_{0.56}$, $\mathbf{Zn}^{\mathrm{D}}_{0.52}$, and $\mathbf{Zn}^{\mathrm{D}}_{0.95}$ are tabulated in Table S9. The $\mathbf{Zn}^{\mathrm{H}}_{0.56}$ data sets were measured at APS beamline 15-ID, while the $\mathbf{Zn}^{\mathrm{D}}_{0.52}$ and $\mathbf{Zn}^{\mathrm{D}}_{0.95}$ data sets were collected at ALS beamline 12.2.1.

TABLE S9: X-ray energies (in keV) used for anomalous diffraction data collection

Sample			Cu K-edge						Zn K-edge		
$\mathbf{Zn}^{\mathrm{H}}_{0.56}$	8.835	8.935	8.985	9.035		9.322		9.609	9.659	9.709	9.809
$\mathbf{Zn}^{\mathrm{D}}_{0.52}$	8.830	8.930	8.980	9.030		9.320	9.410	9.610	9.660	9.710	9.810
$\mathbf{Zn}^{\mathrm{D}}_{0.95}$	8.837	8.937	8.987	9.037	9.137	9.326	9.515	9.615	9.665	9.715	9.815

IV. SIMULATED AND EXPERIMENTAL XANES SPECTRA OF ZN-SUBSTITUTED BARLOWITE AND HERBERTSMITHITE

Summed Cu L-edge data for $\mathbf{Zn}^{\mathrm{H}}_{0.56}$, not shown in the main text, is plotted in Figure S2A. The high resolution transition edge sensor (TES) detector of beamline 10-1 at SSRL records RIXS maps that allow for different emitted energies to be isolated. This separation and energy resolution are required to be able to measure satisfactory Zn L-edge spectra for the barlowite and herbertsmithite families. The Cu L-edge contributes a high fluorescent background that makes the Zn signal impossible to isolate from the total fluorescent yield (TFY) signal, as illustrated in Figure S3 for $\mathbf{Zn}^{\mathrm{H}}_{0.95}$. Elastic scattering also contributes significantly to the TFY. Without the emitted energy discrimination afforded by the TES, usable XAS spectra at the Zn L-edge would be inaccessible for these Cu-containing samples.

The TES also permits separation of the L_3 and L_2 edges, as discussed in the main text and shown in Figure 6. The separated Zn L-edge data for $\mathbf{Zn}^{\mathrm{H}}_{0.56}$ and herbertsmithite are shown in Figure S2B and C along with the summed data. This separation allows the otherwise obscured L_2 edge to be seen clearly.

A covalency analysis was performed on the Cu L-edge spectra following the procedures outlined in Refs. [5] and [6] to measure the Cu character of the hole in the Cu d-band. Cs_2CuCl_4 was used as a covalency calibrator, with the experimental Cu character set at 74%. Cu L-edge spectra were processed by fitting a constant slope to the pre-edge, which was removed from the entire spectrum. Then, spectra were normalized by setting the post-edge to 1 at 990 eV. The continuum edges were subtracted using error functions centered at 943.5 and 963.5 eV. The area of the spectrum was integrated between 920 and 936 eV and between 947 and 957 eV to capture just the $3d$ states. Several standards, listed in Table S10, were measured in order to probe different coordination environments of nominally Cu^{2+} cations.

The calculated partial density of states (DOS) of idealized barlowite, $\mathbf{Zn}_{0.95}$, and herbertsmithite are shown in Figure S4. The Fermi energy (E_{F}) for each compound was shifted to align the top of the valence band with 0 eV. A magnified view of the unoccupied states is shown in Figure S5. Calculations of the partial DOS were performed with Quantum Espresso using the same parameters reported in the main text and a denser $8 \times 8 \times 8$ k-point mesh. To compare with the experimental covalency analysis, the character of the unoccupied states was determined by integrating the Cu and O partial DOS between 1.35–2.8 eV for barlowite and $\mathbf{Zn}_{0.95}$ and 1.75–2.95 eV for herbertsmithite; the results are reported in Table S10. Since the barlowite simulation was done for the room temperature high-symmetry structure, it can be compared to both variants (**1** and **2**) since the measurements were performed at $T = 300$ K. The partial DOS of the Cu^{2+} standards were not calculated in this work; a comparison value was found in the literature for Cs_2CuCl_4. The calculated and experimental values are consistent with each other for all materials.

To investigate the physical origins of the two Zn L-edge peaks near ≈1023 eV and ≈1026.5 eV (see Figure 6 in the main text), core-excited final-state electron density isosurfaces were calculated for both near-edge regions using the "interlayer Zn" models, in which the kagome lattice is fully occupied by Cu^{2+} and the interlayer site is fully occupied by Zn^{2+}. These iso-

surfaces for idealized Zn-substituted barlowite and herbertsmithite are displayed in Figure S6. The isosurfaces corresponding to the first excitation peak in $\mathbf{Zn}_{0.95}$ and herbertsmithite (calculated respectively at 1022.9 and 1023.2 eV) as well as the second excitation peak (calculated respectively at 1026.4 and 1027.2 eV) are shown. The polarization directions for the first set of excitation peaks were chosen to be in-plane (a). For the second set of excitation peaks, in-plane polarization was used for $\mathbf{Zn}_{0.95}$ while out-of-plane (c) polarization was used for herbertsmithite. This was based on an analysis of the transition dipole moments along each of the polarization axes.

The first excitation region (≈1023 eV) is compared in Figure S6A and B: the electron density in both compounds is dominantly coincident with neighboring atoms, consistent with both spectra exhibiting a peak at this energy. No significant difference is seen between the two compounds in this first peak region, whereas in the second peak region (≈1026.5 eV) a larger discrepancy is observed between the two compounds. In the second excitation region, Zn-barlowite exhibits interstitial-dominant electron density while herbertsmithite has site-dominant electron density: the majority of the electron density in pseudo-octahedral herbertsmithite (Figure S6D) lies within the kagome planes above and below the interlayer Zn^{2+} site, while in trigonal prismatic Zn-barlowite it forms large lobes in the interstitial space towards the Br^- atoms (Figure S6C). This reflects the emergence or significant enhancement of the second Zn L-edge XANES peak at ≈1026.5 eV in Zn-barlowite. Note that the excitations in Zn-barlowite have the same major polarization contribution for both peaks, namely in-plane (a), whereas for herbertsmithite the second excitation has out-of-plane (c) polarization. We note that at the Zn L-edge, XANES primarily probes the unoccupied Zn $4s$ states. As the Zn $4s$ orbital is very diffuse, in condensed phase crystals it lacks a clear atomic orbital structure that, for example, the more localized Cu $3d$ orbital would have. Nevertheless, as shown in Figure S6, the electron density associated with XANES final states qualitatively reflects the symmetry of the corresponding excitation peaks.

TABLE S10: Measured and calculated covalency parameters

Sample	L_2 + L_3 Area	Experimental % Cu $3d$ per hole	Calculated % Cu $3d$ per hole	Calculated % O $2p$ per hole	Calculation Ref.
CuO	7.06	62.01	–	–	n/a
Barlowite **1**	9.11	61.71	65.7	31.9	this work
Barlowite **2**	9.04	61.23	65.7	31.9	this work
$\mathbf{Zn}^{\mathrm{H}}_{0.56}$	8.80	59.65	–	–	n/a
$\mathbf{Zn}^{\mathrm{H}}_{0.95}$	8.84	59.89	64.6	32.7	this work
Herbertsmithite	9.15	62.01	64.48	32.78	this work
CuF_2	10.18	68.99	–	–	n/a
$Cu_2(OH)_2CO_3$	9.70	65.75	–	–	n/a
Cs_2CuCl_4	10.92	74.00	72	–	[6]

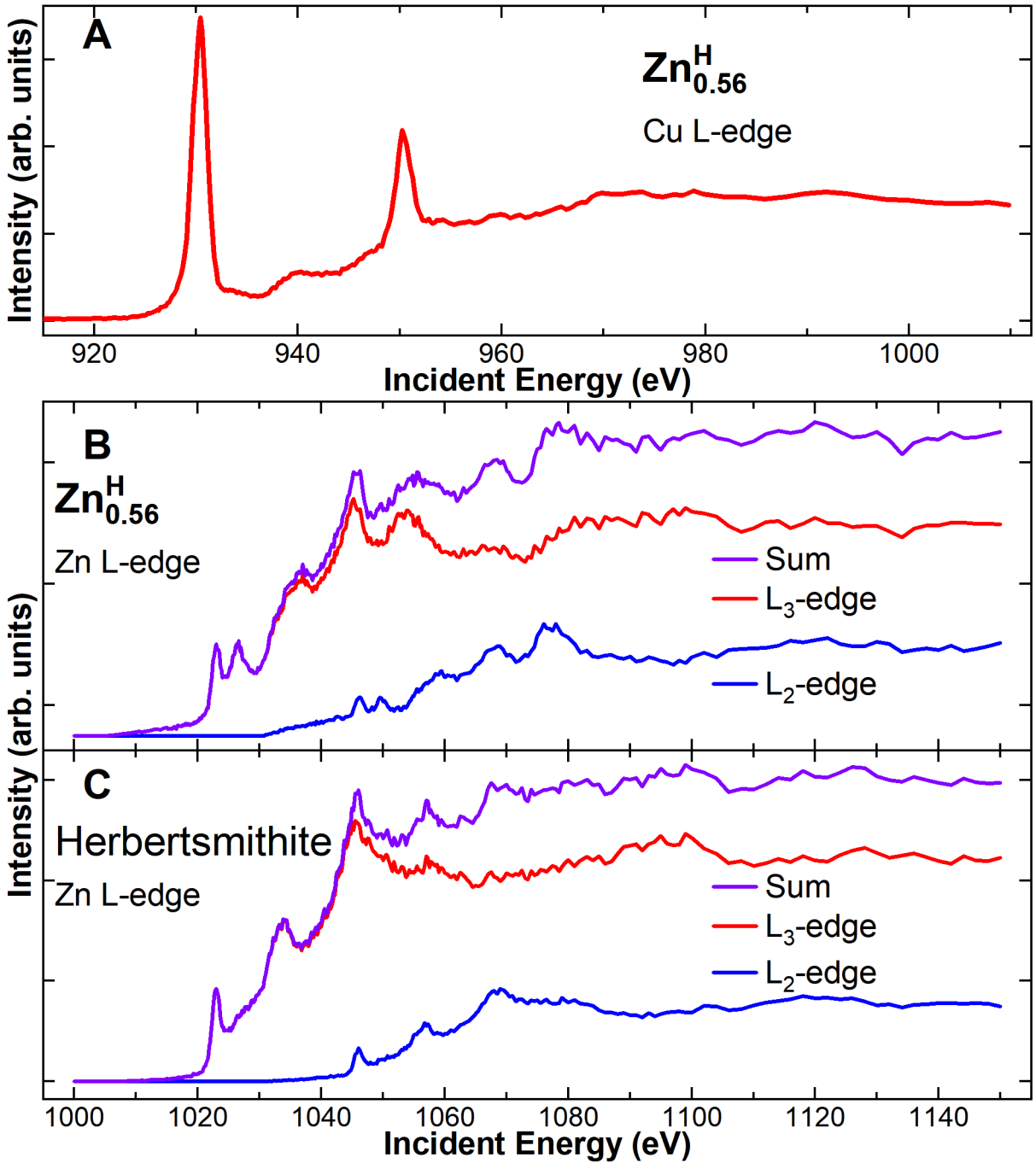

FIG. S2: A) Cu L-edge XANES spectra of $\mathbf{Zn}^{\mathrm{H}}_{0.56}$ measured at $T = 300$ K. Zn L-edge XANES spectra of B) $\mathbf{Zn}^{\mathrm{H}}_{0.56}$ and C) herbertsmithite measured at $T = 300$ K. The separated L_2 and L_3 data are shown along with the summed data.

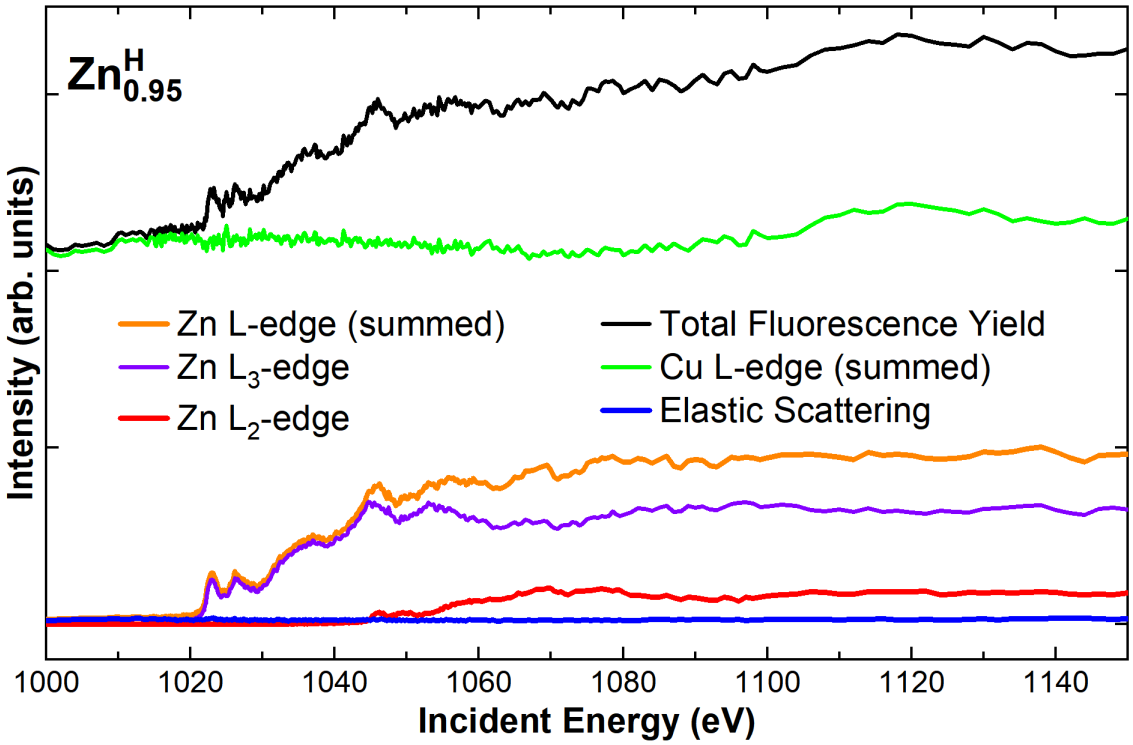

FIG. S3: Zn L-edge XANES spectra of $\mathbf{Zn}^{\mathrm{H}}_{0.56}$ measured at $T = 300$ K. The raw total fluorescence yield data is shown along with the various contributions that can be isolated using the energy resolution of the TES detector: the fluorescent background from the Cu L-edge, the Zn L-edge signal (summed and separated into L_2 and L_3 contributions), and the elastic scattering contribution.

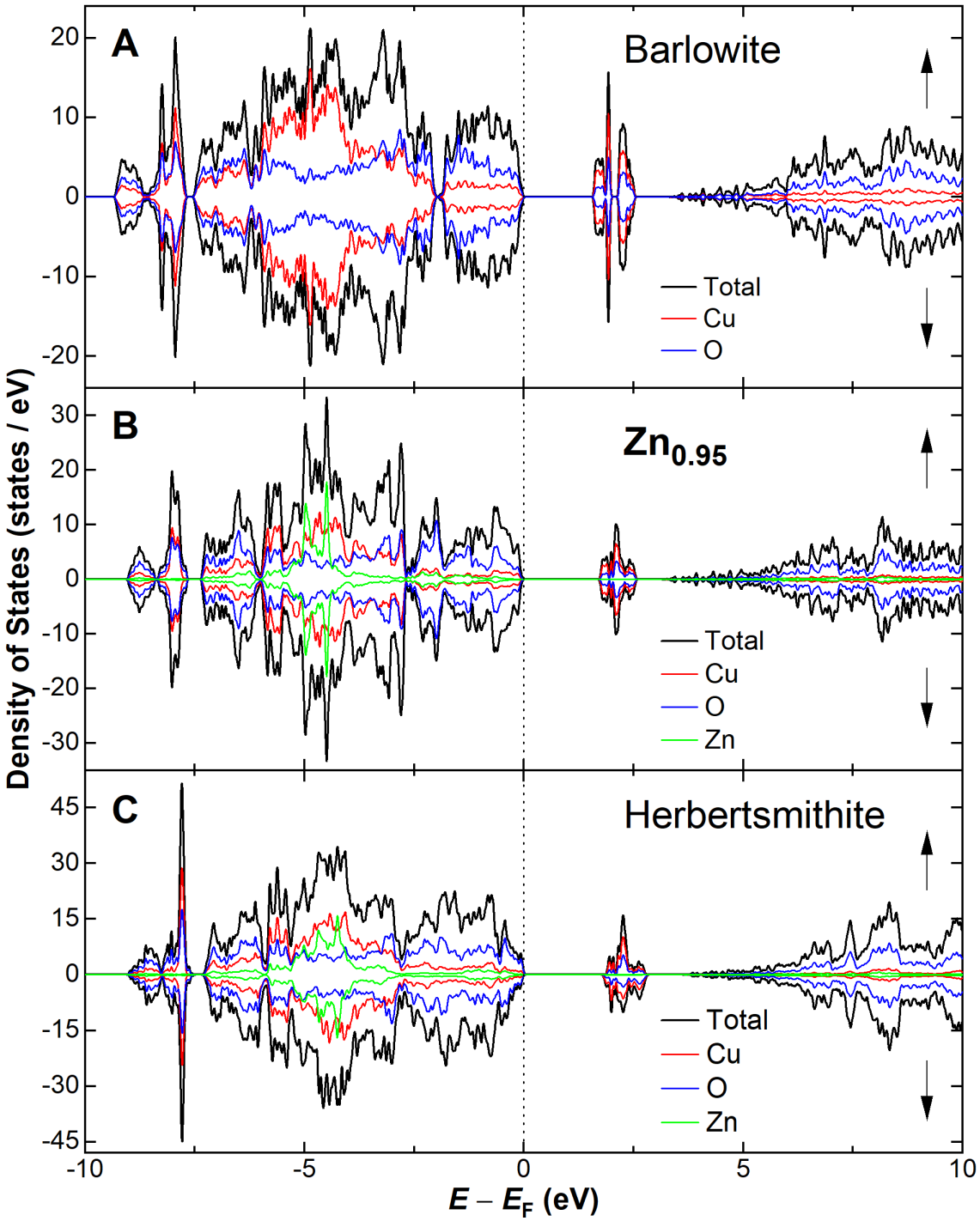

FIG. S4: Partial density of states (DOS) of A) room temperature (high-symmetry hexagonal) barlowite, B) $\mathbf{Zn}_{0.95}$, and C) herbertsmithite. The Fermi energy (E_{F}) for each compound was shifted to align the top of the valence band with 0 eV.

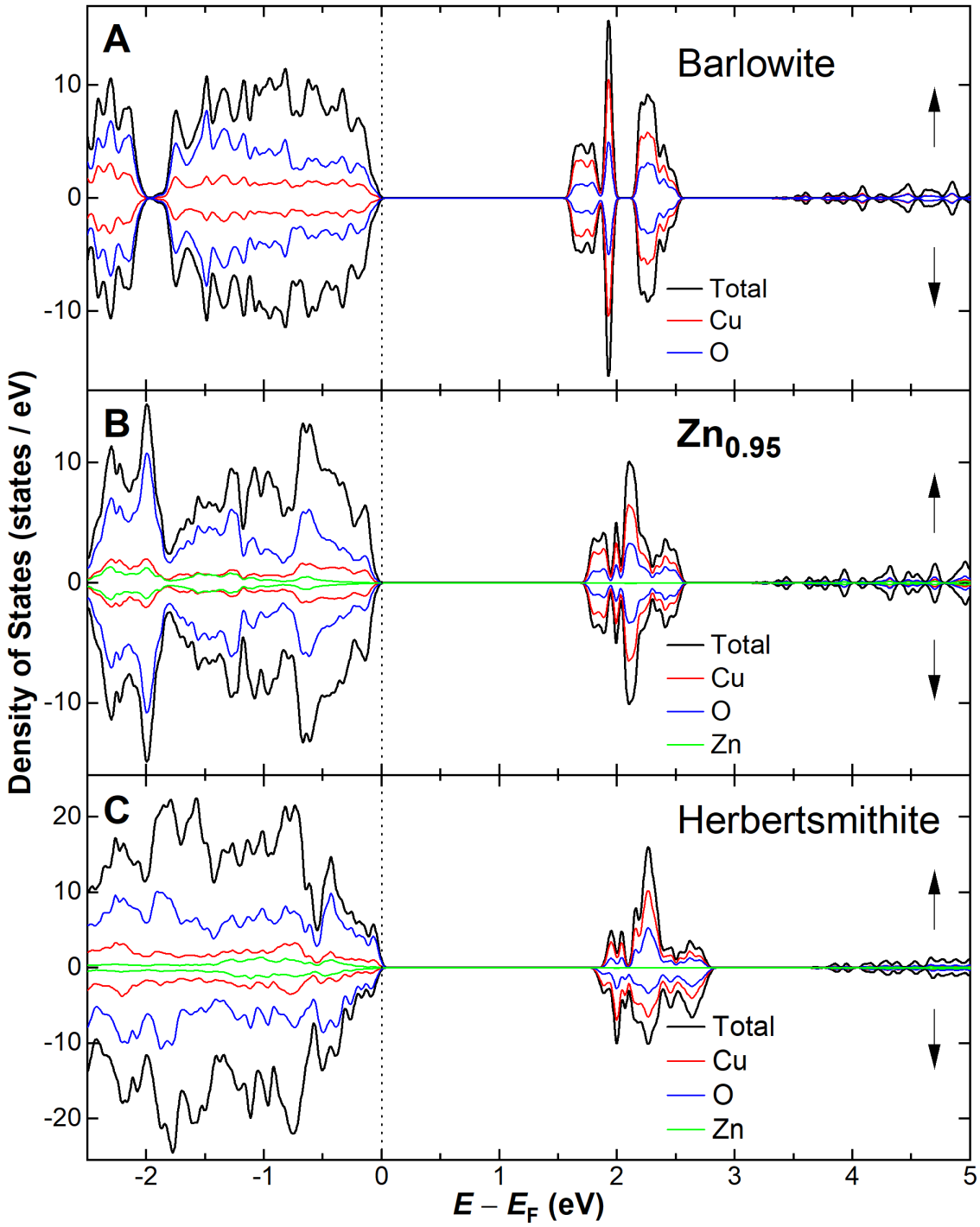

FIG. S5: Magnified view of the partial density of states (DOS) around the unoccupied states. A) Room temperature (high-symmetry hexagonal) barlowite, B) $\mathbf{Zn}_{0.95}$, and C) herbertsmithite.

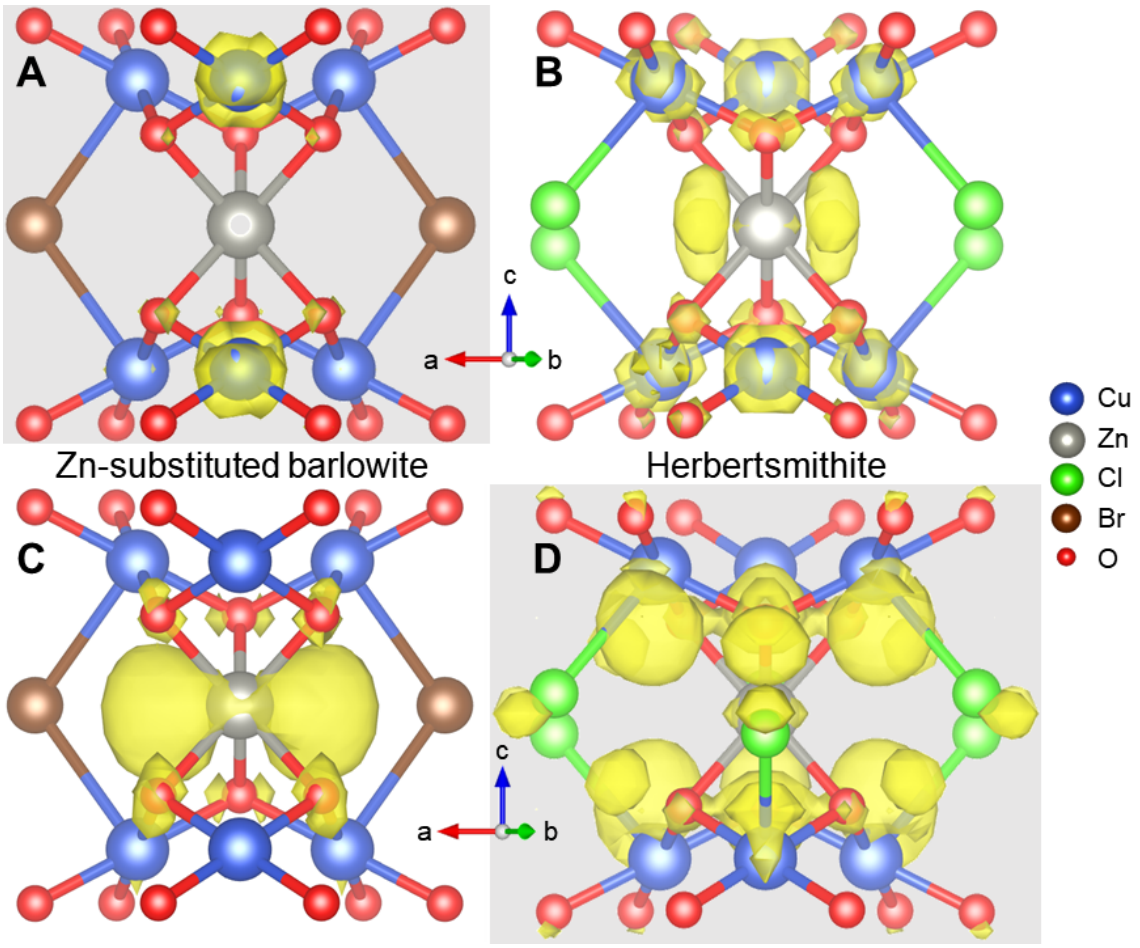

FIG. S6: A) and B) Electron density isosurfaces calculated for the lowest energy excitation peak of the respective "interlayer Zn" models of A) Zn-substituted barlowite $\mathbf{Zn}_{0.95}$ (1022.9 eV) and B) herbertsmithite (1023.2 eV) at an isosurface level of 10%. C) and D) Bubble plots of electron density calculated for the second lowest energy excitation peak of the respective "interlayer Zn" models of C) Zn-substituted barlowite $\mathbf{Zn}_{0.95}$ (1026.4 eV) and D) herbertsmithite (1027.2 eV) at an isosurface level of 15%. For clarity, H and F atoms are not shown. The structures are visualized in VESTA.[7]

V. SIMULATED AND EXPERIMENTAL XANES SPECTRA OF SR_3ZNRHO_6 AND ZNF_2

To check if the trend observed in Zn-substituted barlowite and herbertsmithite (a single XANES peak for pseudo-octahedral coordination versus two peaks for trigonal prismatic coordination) is systematic, we performed analogous simulations on materials with similar Zn^{2+} coordination environments. The interlayer coordination in herbertsmithite is reasonably close to cubic, so we chose rutile ZnF_2, in which Zn^{2+} is six-coordinate and locally cubic. As shown in Figure S7, the Zn L-edge spectra of ZnF_2 indeed display a single peak at ≈1024 eV in both the simulation and the experimental XANES data, similar to herbertsmithite. We simulated a spectrum for Sr_3ZnRhO_6,[8] one of the few materials in which Zn^{2+} is trigonal prismatic besides Zn-barlowite, and it displays a distinct two-peak structure at low energy (≈1024 and ≈1026 eV). The calculated partial DOS of ZnF_2 and Sr_3ZnRhO_6 are shown in Figure S8. The Fermi energy (E_F) for ZnF_2 was aligned so the top of the valence band is at 0 eV. The partial DOS of both compounds are in good agreement with those calculated by the Materials Project.[9]

Calculated electron density isosurfaces of both compounds (Figure S9) confirm the trend seen in Zn-substituted barlowite and herbertsmithite. They were calculated for the two excitation peak regions observed in the experimental and simulated spectra of Sr_3ZnRhO_6 and ZnF_2. The first excitation peak was calculated at 1023.97 and 1023.83 eV for Sr_3ZnRhO_6 and ZnF_2, respectively, while the second excitation peak was calculated at 1025.95 and 1024.8 eV, respectively. The first excitation region (≈1024 eV) is compared in Figure S9A and B, showing a similar pattern of diffuse electron density for both compounds. This is consistent with both XANES spectra exhibiting a peak at the same energy. However, the second excitation region (≈1026 eV) exhibits a difference: the electron density in ZnF_2 lies mostly along the Zn–F bonds, while in Sr_3ZnRhO_6 it arises as large lobes towards unoccupied interstitial areas of the unit cell. This behavior is consistent with that observed in the Zn-substituted barlowite and herbertsmithite electron density isosurface comparison (Figure S6), and it confirms the correlation between the loss of inversion symmetry and an added peak in the XANES spectra. The polarization directions for both excitation peaks in both compounds were chosen to be in-plane (a). This was based on an analysis of the transition dipole moments along each of the polarization axes.

Thus, the simple one-peak spectrum appears to be characteristic of 6-coordinate Zn^{2+} with a locally cubic or pseudo-cubic/pseudo-octahedral environment, and the second prominent peak observed in ZnF_2 and Zn-barlowite results from the trigonal prismatic coordination and the subsequent loss of inversion symmetry.

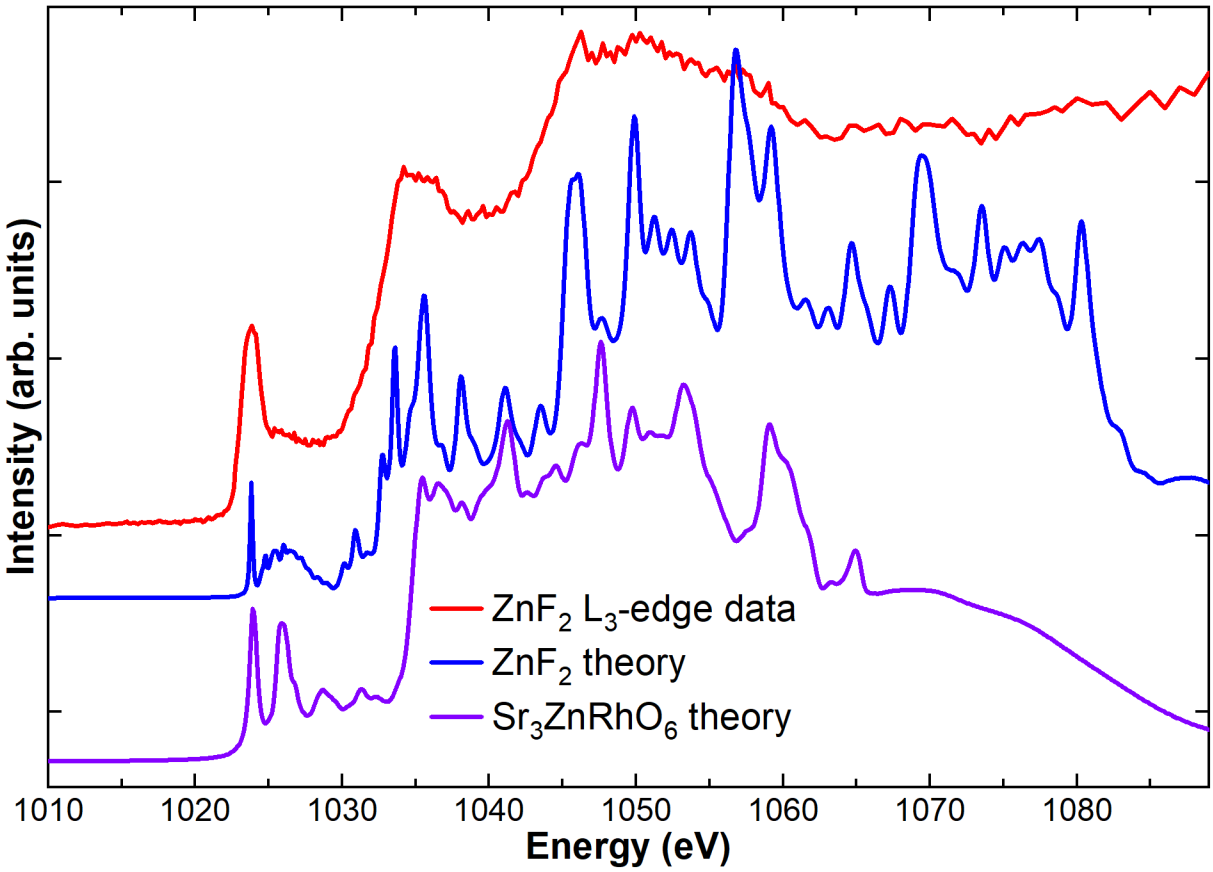

FIG. S7: Zn L_3-edge XANES data of ZnF_2 measured at $T = 300$ K and calculated spectra of ZnF_2 and Sr_3ZnRhO_6. No broadening has been applied to the simulated spectra. Vertical offsets have been applied to separate the spectra.

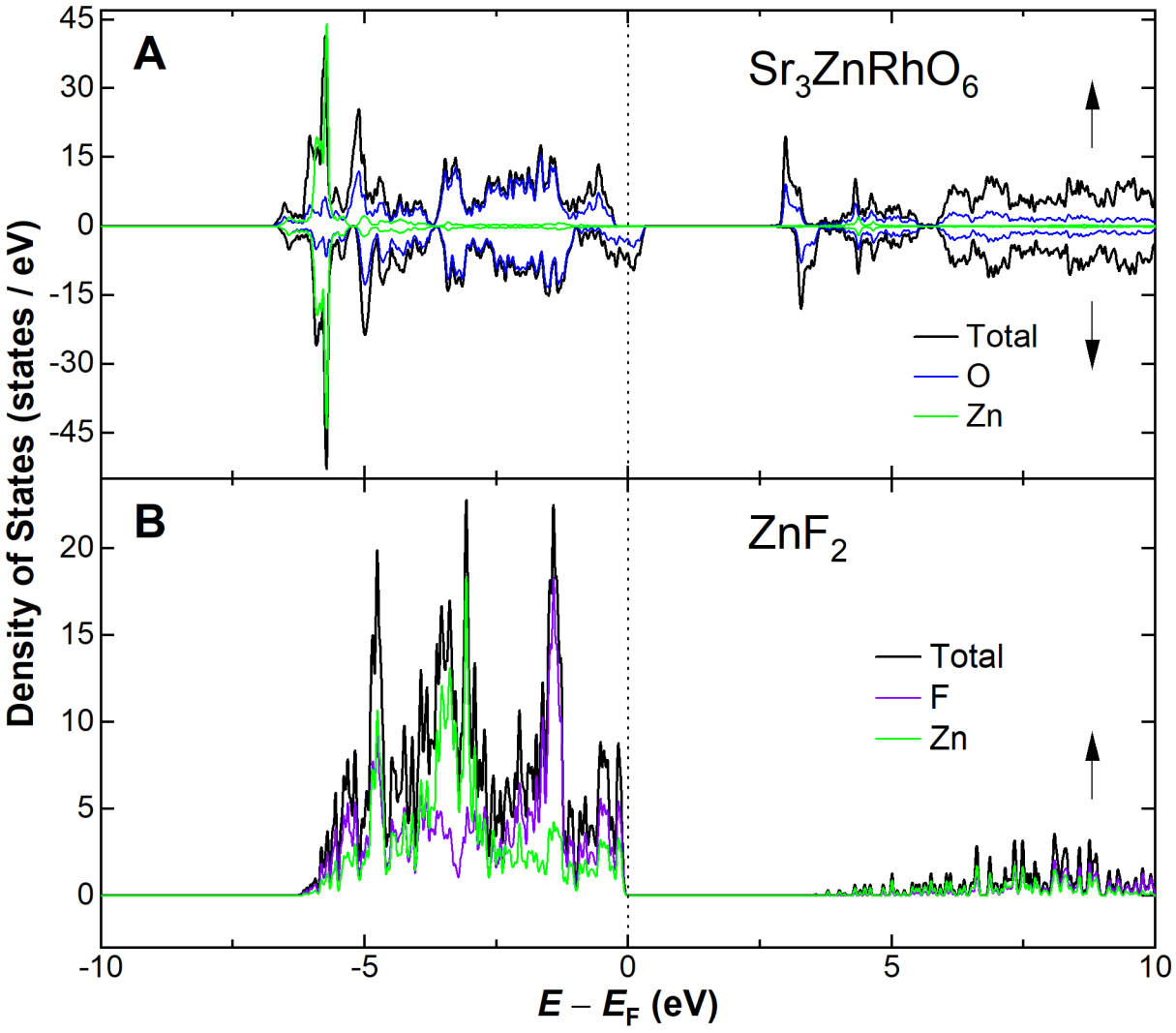

FIG. S8: Partial density of states (DOS) of A) Sr_3ZnRhO_6 and B) ZnF_2. The Fermi energy (E_F) for ZnF_2 was aligned so the top of the valence band is at 0 eV.

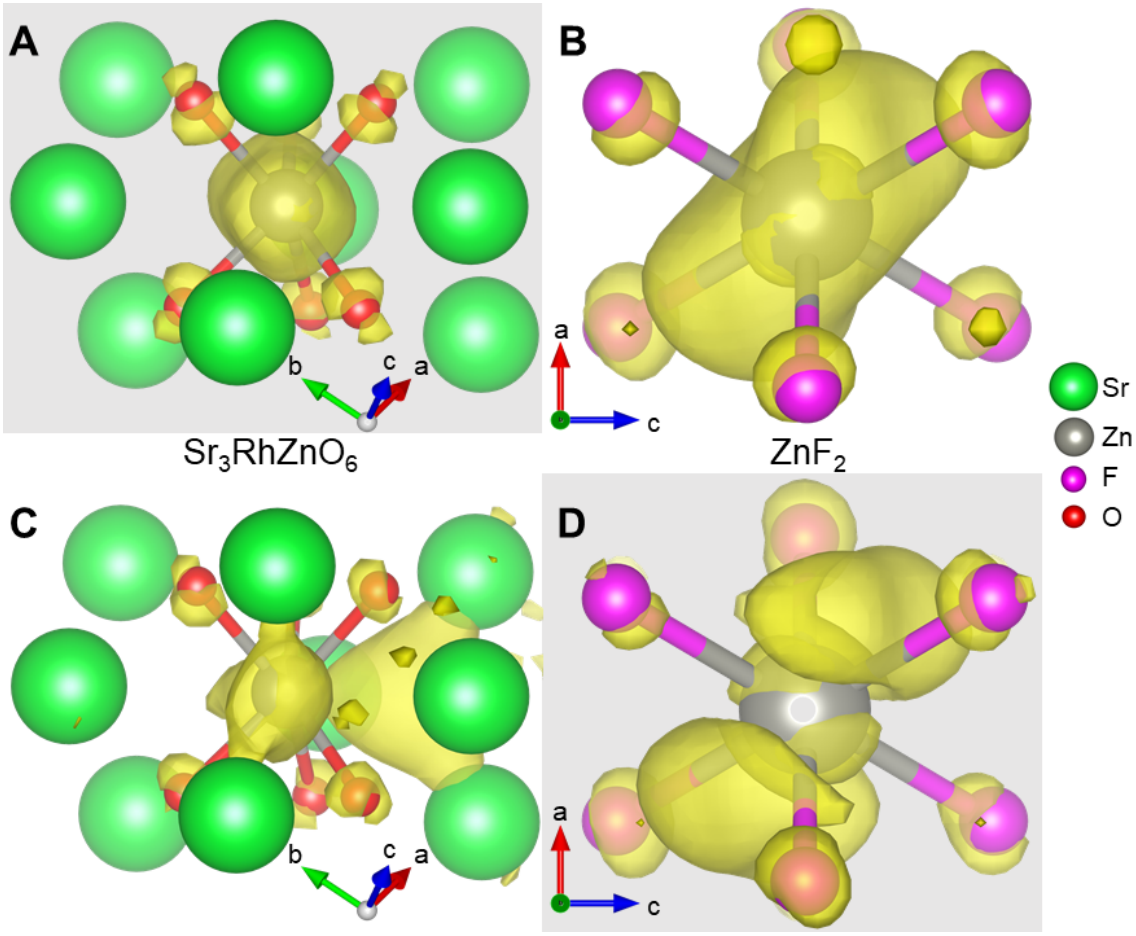

FIG. S9: A) and B) Electron density isosurfaces calculated for the lowest energy peak of A) trigonal prismatic Sr_3ZnRhO_6 (1023.97 eV) and B) cubic ZnF_2 (1023.83 eV) at an isosurface level of 10%. C) and D) Bubble plots of electron density calculated for the second lowest energy peak of the respective "interlayer Zn" models of C) Sr_3ZnRhO_6 (1025.95 eV) and D) ZnF_2 (1024.8 eV) at an isosurface level of 15%. The structures are visualized in VESTA, and Rh is omitted for clarity.[7]

[1] G. M. Sheldrick, Crystal structure refinement with SHELXL, Acta Crystallogr. C **71**, 3 (2015).

[2] O. V. Dolomanov, L. J. Bourhis, R. J. Gildea, J. A. K. Howard, and H. Puschmann, *OLEX2*: A complete structure solution, refinement, and analysis program, J. Appl. Crystallogr. **42**, 339 (2009).

[3] B. H. Toby and R. B. Von Dreele, *GSAS-II*: the genesis of a modern open-source all purpose crystallography software package, J. Appl. Crystallogr. **46**, 544 (2013).

[4] B. Ravel and M. Newville, *ATHENA*, *ARTEMIS*, *HEPHAESTUS*: data analysis for X-ray absorption spectroscopy using *IFEFFIT*, J. Synchrotron Radiat. **12**, 537 (2005).

[5] S. J. George, M. D. Lowery, E. I. Solomon, and S. P. Cramer, Copper L-Edge Spectral Studies: A Direct Experimental Probe of the Ground-State Covalency in the Blue Copper Site in Plastocyanin, J. Am. Chem. Soc. **115**, 2968 (1993).

[6] I. M. Dimucci, J. T. Lukens, S. Chatterjee, K. M. Carsch, C. J. Titus, S. J. Lee, D. Nordlund, T. A. Betley, S. N. MacMillan, and K. M. Lancaster, The Myth of d^8 Copper(III), J. Am. Chem. Soc. **141**, 18508 (2019).

[7] K. Momma and F. Izumi, *VESTA 3* for three-dimensional visualization of crystal, volumetric and morphology data, J. Appl. Crystallogr. **44**, 1272 (2011).

[8] R. Layland and H. zur Loye, Synthesis, characterization, and magnetic properties of a commensurate and incommensurate phase of Sr_3ZnRhO_6: zinc in trigonal prismatic coordination, J. Alloys Compd. **299**, 118 (2000).

[9] A. Jain, S. P. Ong, G. Hautier, W. Chen, W. D. Richards, S. Dacek, S. Cholia, D. Gunter, D. Skinner, G. Ceder, and K. A. Persson, Commentary: The Materials Project: A materials genome approach to accelerating materials innovation, APL Mater. **1**, 011002 (2013).